Design and Test of a Radio-Frequency Electrothermal Thruster

A Major Qualifying Project Report
Submitted to the Faculty of the
WORCESTER POLYTECHNIC INSTITUTE
in Partial Fulfillment of the Requirements for the
Degree of Bachelor of Science
in Aerospace Engineering

by

[signature]

Abigail Cervelloni

[signature]

Jared Kepron

[signature]

Ian Limon

[signature]
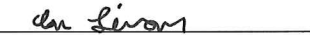
Christian Zelaya

March 18, 2016

Approved by: *[signature]*

Professor John J. Blandino, Advisor
Aerospace Engineering Program
Mechanical Engineering Department, WPI

Table of Contents

ABSTRACT

The goal of this project was to design, build, and test a radio-frequency electrothermal thruster (RFET) to operate on argon over a power range of 400-600 W at a frequency of 13.56 MHz. The RFET was designed for testing in a vacuum chamber operating in the millitorr range. The RFET required a complete redesign from a previously fabricated model. An impedance matching network was designed and constructed to maximize the power delivered to the discharge. The matching network, installed in the vacuum chamber, was designed to allow tuning by use of a motor-driven variable capacitor. A stand was designed and constructed to secure the RFET and matching network within the vacuum chamber. This paper reports on the design, fabrication, assembly, and test of the RFET and matching network.

LIST OF FIGURES

LIST OF TABLES

ACKNOWLEDGEMENTS

TABLE OF AUTHORSHIP

Section	Author
Introduction	AC, JK
Background	
2.1, 2.2, 2.3	JK
2.4	AC
2.5	CZ
2.6	IL
Methodology	
3.1, 3.5.3	JK
3.2, 3.7	AC
3.3, 3.4, 3.5.1, 3.5.2	CZ
3.6	IL
Results & Discussion	JK
Conclusion & Recommendations for Future Work	IL, AC, JK

1. INTRODUCTION

Radio-frequency electrothermal thruster (RFET) technology shows great promise for the future of spacecraft propulsion. Electric propulsion systems use electrical energy, rather than chemical reactions, to generate thrust. An electrothermal thruster is a type of electric propulsion system that uses electromagnetic fields to partially ionize an inert gas, such as argon or xenon, into a plasma state. The resulting increase in temperature further pressurizes the contained gas, which is then accelerated through a nozzle, thereby generating thrust. In the case of RFET technology, the neutral gas is ionized through collisions with electrons that have been accelerated through electric fields generated by an RF antenna.

While electrothermal thrusters do not produce high thrust, they can use propellant much more efficiently than chemical thrusters, having been demonstrated to match and even exceed the specific impulse[1] values typical of common chemical propulsion systems [1]. These low thrust and high specific impulse characteristics make RFET technology ideal for orbital correction maneuvers, where minute changes are necessary. Additionally, RFET technology boasts mechanical simplicity over common chemical propulsion systems, requiring only a discharge chamber tube filled with inert gas, a radio frequency antenna to excite the gas into plasma, and a nozzle through which to accelerate the pressurized chamber contents. However, one disadvantage of this technology is that a vacuum environment is required for ground testing in order to create a sufficiently low back pressure. The chamber pressure, corresponding to the volume where the RF power is coupled, is subatmospheric in order to sustain the plasma at power levels on the order of a few hundred watts.

Figure 1 shows the thruster that was designed, built, and tested for this project. The gas is introduced into a sealed quartz tube and is heated by an alternating current carrying wire wrapped around the quartz tube. The current is provided by a radio-frequency power supply, operating at 13.56 MHz. Inert gases with low molecular weights are commonly used for the generation of plasma in electrothermal thrusters. Argon was selected by 2015 RFET team [1] as the propellant gas because it is relatively inexpensive and safe to use. The heated argon is then accelerated out the nozzle at the end of the thruster chamber.

---

[1] Specific impulse (Isp) is defined as thrust per unit propellant weight flow rate.
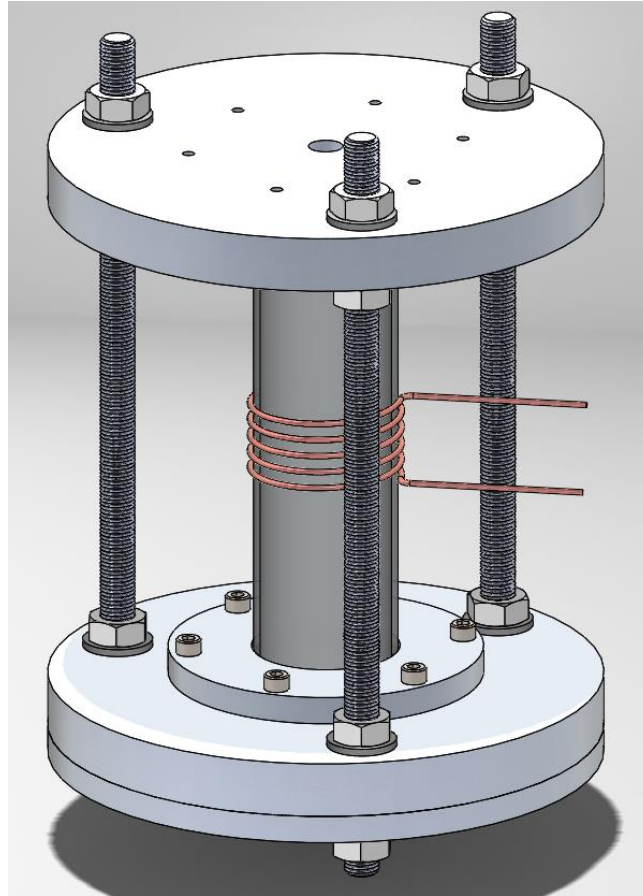
Figure 1. Radio Frequency Electrothermal Thruster Design.

With a budget of $800, the 2016 RFET MQP team was tasked with fabricating a fully functional radio-frequency electrothermal thruster using the groundwork set by the 2015 RFET team [1]. The 2016 project included the design, assembly, and test of the matching network box, design and construction of the RF antenna, complete redesign and fabrication of the mechanical thruster assembly, and construction and integration of a stand to secure the thruster during testing. Testing was conducted to demonstrate that a discharge could be ignited and to evaluate the matching network designed and built for the project. This thruster will serve as a proof-of-concept example for future research at Worcester Polytechnic Institute (WPI).

2. BACKGROUND

2.1 Plasma as a State of Matter

One of the four fundamental states of matter, plasma exhibits characteristics very unlike the other three fundamental states – these being gas, liquid, and solid. Namely, while gases, liquids, and solids are composed solely of molecules subject to intermolecular bonds and (in the case of crystalline solids) specific configurations, plasmas consist of ions and electrons. In a partially ionized plasma, neutral species are also present. The species in a partially ionized plasma can include dissociated ions, electrons, excited molecules, and molecular fragments [2]. Figure 2 qualitatively illustrates the difference between the fundamental states [3].
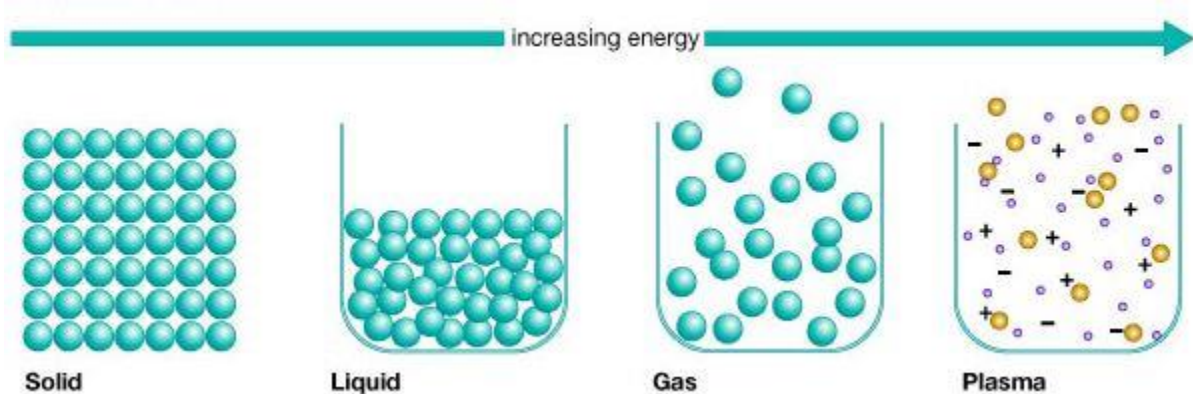
Figure 2. The four fundamental states of matter [3]. © 2011 Encyclopedia Britannica, Inc.

As can be seen in Figure 2, the molecular dissociation and subsequent ionization that produces a plasma is caused by an addition of energy to a gas, usually resulting from an increase in temperature. Such a rise in temperature can be generated in a number of ways, although for the scope of the RFET project, only radio-frequency excitation was considered.

2.2 Principles of Electrothermal Thruster Operation

In addition to the radio-frequency excited plasma utilized for the RFET project, some common electrothermal thruster variants include arcjets and resistojets. Arcjet thrusters, as shown in Figure 3, use a cathode and anode configuration to produce an arc which transfers

energy to the propellant fluid flowing past [4]. Alternatively, resistojet thrusters, as shown in Figure 4, employ a resistor placed in the flow of propellant to transfer energy to the gas [5]. In both of these cases, there is a resultant increase in energy due to electrical heating, and the propellant is accelerated through an adjacent nozzle. However, only in the case of the arcjet is the increase in temperature and energy significant enough to cause a state transition into plasma.
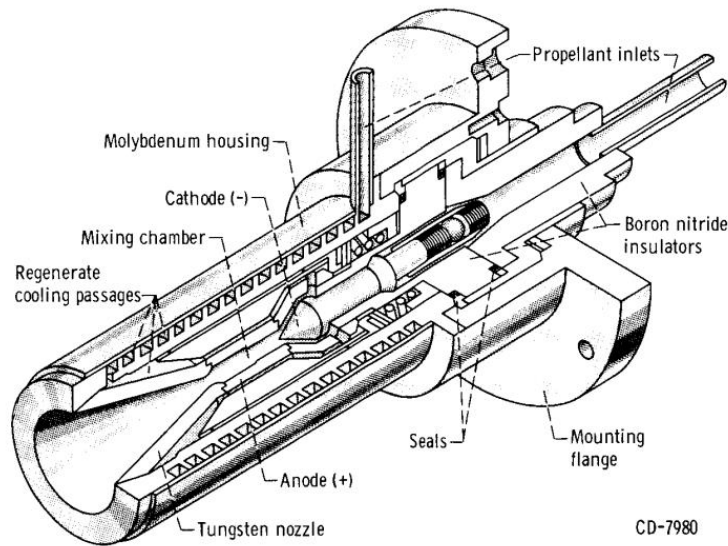
Figure 3. Cutaway view of a 30-kilowatt direct-current regeneratively cooled arc-jet thruster [6]. © 1965 NASA.
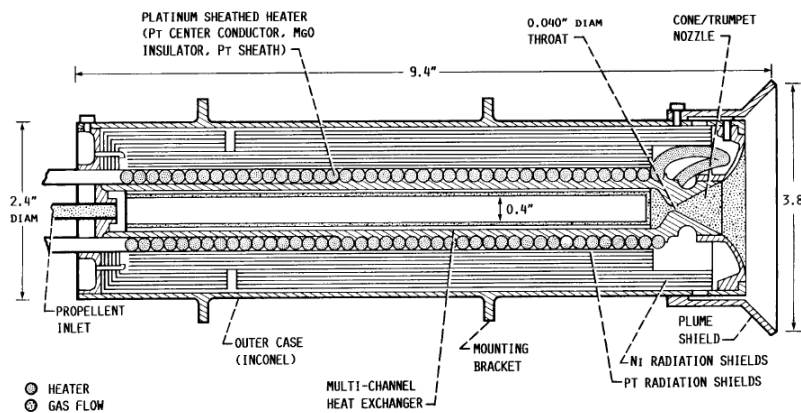
Figure 4. Advanced development engineering model resistojet [7]. © 1987 NASA.

Conversely, radio-frequency electrothermal thrusters use electromagnetic waves to increase the energy of the propellant into the plasma transition regime. This radio-frequency discharge is produced using an antenna coil which carries a current from a radio-frequency source, typically operating at 13.56 MHz, resulting in an inductively coupled plasma [8], as can be seen in Figure 5 [9].
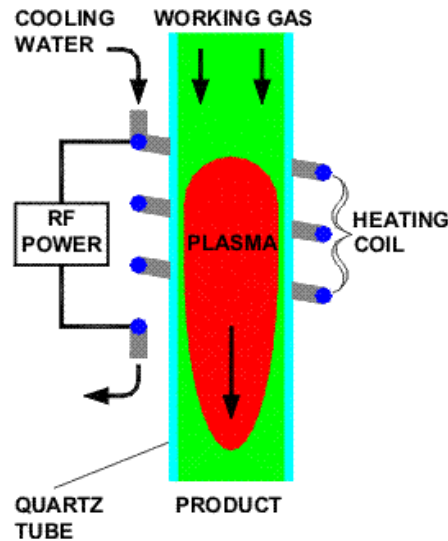
Figure 5. Inductively Coupled RF Plasma Torch [9]. © 1993 National Space Research Institute.

Such inductively coupled plasma discharges generally operate in one of two modes: the capacitive "E" mode or the inductive "H" mode. E mode has both lower plasma density and lower plasma potential relative to H mode. For this reason, H mode discharge is more likely to occur at a higher input power compared to E mode, for a given flow rate [10]. While E mode electron density and light emission are lower than that of H mode, electron temperature is marginally higher for E mode discharge. Despite the lower electron temperature exhibited by H mode discharge, the higher plasma potential results in higher chamber temperature and better power coupling. This is ultimately the product of a more efficient energy transfer between the RF power source and the gas molecules. The E to H mode transition takes place when the power input is increased to a certain value, but the H to E mode transition takes place when the power input is decreased to a certain value lower than that required for the E to H mode transition. This

hysteresis phenomenon means that the H mode can be maintained at a lower power input after it has been initially established. This allows for greater energy transfer efficiency at lower energy input. This is especially important in radio-frequency electrothermal thruster applications since inducing and maintaining H mode discharge directly correlates to generating higher thruster efficiency (i.e. specific impulse) [11].

In radio-frequency electrothermal thrusters, the plasma is contained within a discharge chamber. This chamber is typically a cylindrical tube of quartz or Pyrex (trade name for a borosilicate glass), due to their low loss dielectric and thermal properties [12]. As has been previously mentioned, the plasma within the discharge chamber is excited by a radio-frequency electromagnetic field, produced by a coiled antenna. The energy source for an RF thruster is external to the discharge and, in the case of an inductive discharge, the antenna is separated from the hot gases by the discharge chamber walls. In comparison, arcjet thrusters operate with a cathode which is surrounded by the flowing gas, while resistojet thrusters transfer heat directly to the flow through conduction from heated surfaces. Since the metal antenna coil is insulated from the discharge chamber gases, it is more resistant to wear from exposure to heated propellant gas.

In order to maintain sufficient pressure in the discharge chamber, end plates seal each end of the discharge tube. One of these end plates features an inlet for propellant gas to be introduced into the discharge chamber, while the opposite end plate features a nozzle, through which the propellant is able to escape, thus generating thrust. The gas flow rate and orifice (nozzle throat) diameter is chosen such that the pressure in the discharge chamber remains within an acceptable range, allowing the discharge to be sustained while producing a desired constant level of thrust. Another advantage of radio-frequency electrothermal thrusters is that the construction is relatively simple, consisting of only the discharge tube, antenna, radio-frequency power source, and basic housing components. While not trivial, such a system is less complicated overall than the chemical propulsion systems commonly found onboard modern spacecraft.

2.3 Previous RFET Technologies

While there have been a number of successfully assembled radio-frequency electrothermal thrusters, few of these efforts are well documented, particularly with regard to precise hardware specifications. While this lack of substantial documentation hinders current

attempts at replicating the successful builds, some technical details can be gathered from the various reports.

One example is a radio-frequency electrothermal thruster designed at Pennsylvania State University. This thruster, the design of which can be seen in Figure 6, was a low power model, operating consistently with an input power of 100 W. However, an AL-1200 radio-frequency amplifier was used to increase the power input to roughly 140 W in order to initiate H mode discharge before reducing power to the 100 W operating condition. The antenna, which was wrapped around the quartz chamber tube approximately 14 times, was made from 18 AWG magnet wire. Helium gas, injected tangentially into the chamber at variable mass flow rates (ranging from 0.43 mg/s to 1.08 mg/s), was used as propellant for this thruster. The primary research completed with this thruster was in studying the power necessary for E and H mode transitions. As mentioned previously, the findings were that 140 W was required to transition from E to H mode, which could then be maintained with power decreased to as low as 100 W [11].
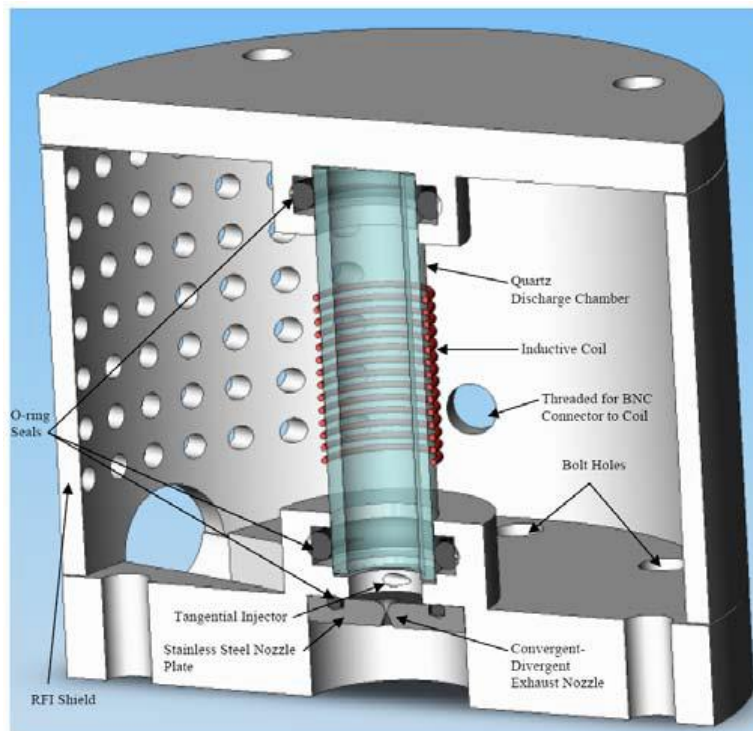
Figure 6. RFET Sample Design [11]. © 2009 the Authors.

While the report published by the Penn State group detailed a fair amount qualitatively, it lacked quantitative definition of the construction parameters and specifications. Therefore, additional research on radio-frequency electrothermal thruster assembly was required.

A paper published as a joint effort between groups at the Australian National University and the United Kingdom's York Plasma Institute provided better dimension specifications [13]. However, this thruster, nicknamed the "Pocket Rocket", was significantly smaller than desired – the discharge chamber tube measuring just 2 cm in length and 4.2 mm in diameter. Unlike the Penn State group, however, this effort used argon gas as propellant, with a less common 12.50 MHz radio-frequency source. A diagram of this thruster can be seen in Figure 7.
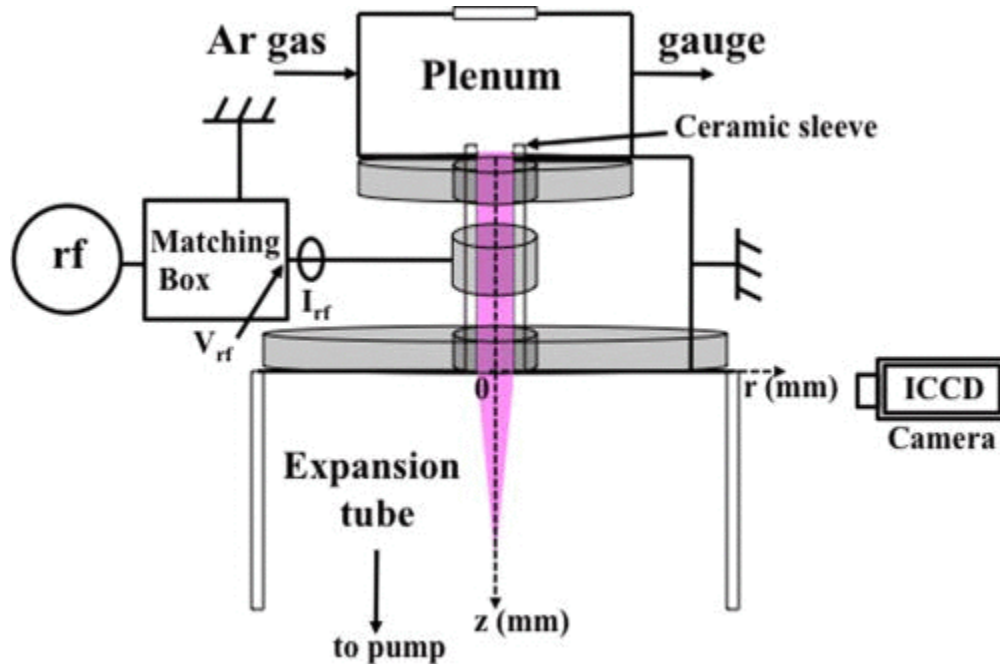
Figure 7. "Pocket Rocket" Design [13]. © 2013 the Authors.

A similar partnership between the Australian National University and Japan's Iwate University focused on thrust measurements of a radio-frequency electrothermal thruster system [14]. Two discharge chamber tubes were tested for this thruster configuration, one measuring 17.5 cm in length and another measuring 9.5 cm in length. At 700 W of input power, produced by a 13.56 MHz radio-frequency source, an argon propellant mass flow rate of 0.9 mg/s in the

longer tube generated 2 mN of thrust, while a flow rate of 1.65 mg/s in the shorter tube resulted in 4 mN of thrust. The antenna for this configuration was a length of copper wire wrapped twice around a Pyrex discharge chamber tube with a diameter of 6.4 cm. A schematic of this configuration can be seen in Figure 8. As can be seen in this schematic, a double pendulum structure was used in conjunction with a laser displacement sensor in order to detect and measure the minute thrust values produced. The pendulum allows for free motion of the thruster along the axis of the thrust generated, while the laser sensor measures displacement which can then be used to calculate thrust.
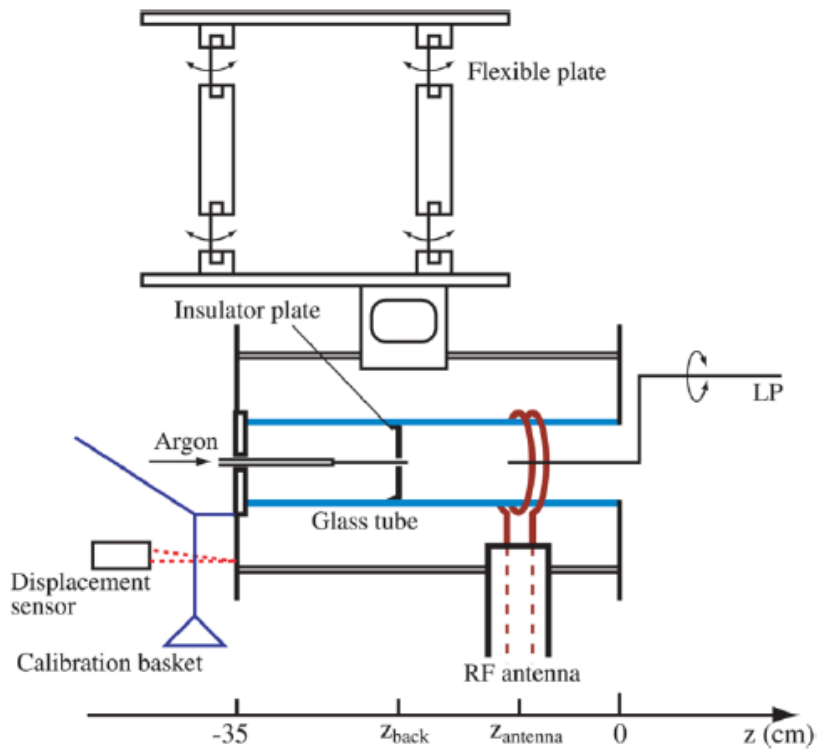
Figure 8. RFET Thrust Measurement Setup [16]. © 2011 the Authors.

2.4 Impedance Matching Network

Impedance is the effective resistance that occurs in electrical circuits operating at high frequencies. The power that can be delivered to an electrical load from an alternating current source, such as a radio-frequency power supply (or "transmitter"), is in large part determined by

this impedance. To describe the impedance mathematically, the "total" value can be decomposed into real and imaginary components. The real component of impedance comes from the resistance of the circuit. The imaginary component stems from the circuit's reactance, induced by capacitance and/or inductance. Capacitors and inductors will affect the phase of the current waveform relative to the voltage waveform differently. For this reason, the impedance induced by a capacitor will have a negative reactance while the impedance induced by an inductor will have a positive reactance.

High impedance is an undesirable characteristic for electrical circuits since it causes a portion of the input power to be reflected back to the power source. This reflection of power can potentially damage the power supply. Additionally, high power reflected means low power delivered. If a low percentage of the input power is being delivered to the load, the system is inefficient in that it will require higher power consumption but operate at lower levels.

To mitigate the negative effects of high impedance, an impedance matching network can be utilized. Impedance matching is the practice of designing the impedance of a circuit to match the impedance of the electrical load. By making the source impedance equal to the load impedance, the power transferred to the load is maximized and the power reflected back to the source is minimized.

One of the simplest types of matching networks is an L-network, which consists of one inductor placed in parallel with the load and one capacitor placed in series with the power supply. L-networks are common in electrical experiments and, according to IEEE Transactions on Circuits and Systems, can be implemented to sufficiently compensate for antenna mismatch from RF power supplies [15]. Figure 9 shows the circuit diagram for an L-type impedance matching network. The capacitor is represented by "C", the inductor is "L", and the impedance of the load is "Z_L".
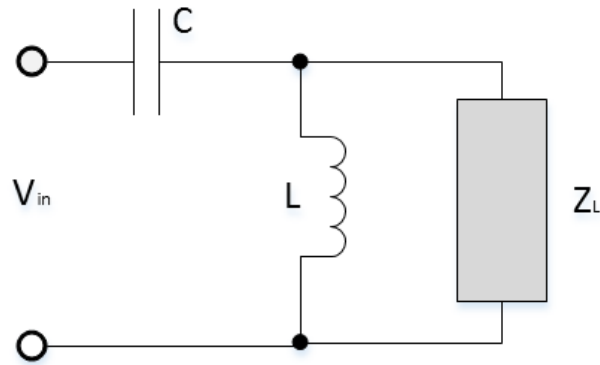
Figure 9. L-Network Circuit Diagram.

Some circuits have impedance values that vary with time. If this is the case, variable electrical components can be integrated into the matching network, allowing for the network to be tuned as impedance values of the circuit fluctuate. Changing the capacitance of a circuit directly alters the overall impedance. The use of variable capacitors has been observed to efficiently couple external power to circuit loads [16].

2.5 RF Antenna

As previously mentioned, in dealing with radio frequency electrothermal thrusters, plasma is generated through electromagnetic induction. This is accomplished by coupling power through an antenna that has been coiled around a discharge chamber.

An 18 American Wire Gauge (AWG), 14-turn coil was used in operation of the RFET constructed by the group from Pennsylvania State University. However, several issues occurred as a result of their material choice and construction methods. After extended operation in H mode, it was found that the insulation of the 18 AWG coil was beginning to experience thermal degradation. A switch to 16 AWG was recommended due to better power handling and heat dissipation properties, according to properties shown in Table 1 [17].

Table 1. American Wire Gauge (AWG) Cable/Conductor Sizes and Properties [17].

AWG	Diameter [inches]	Diameter [mm]	Area [mm^2]	Resistance [Ohms / 1000 ft]	Resistance [Ohms / km]	Max Current [Amperes]	Max Frequency for 100% skin depth
16	0.0508	1.29032	1.31	4.016	13.17248	3.7	11 k Hz
17	0.0453	1.15062	1.04	5.064	16.60992	2.9	13 k Hz
18	0.0403	1.02362	0.823	6.385	20.9428	2.3	17 kHz

The coil used at Penn State was hand wrapped and the individual coils themselves were said to be imprecise in spacing. Due to this imprecision, brighter regions of plasma were observed in the top and bottom of the chamber, indicating an uneven electric field and hence plasma density distribution in the active discharge. It was theorized by the Penn State group that more careful coil construction would lead to a more uniform RF current and magnetic field, which would produce a more uniform plasma distribution. Additionally, Dr. Lynn Olson, senior scientist at the Busek Company, provided some guidance on the coil design. In the correspondence it was advised to reduce the number of turns in the coil design (L. Olsen, personal communication).

The difficulty in designing an antenna coil configuration with impedance mismatch that can be compensated for through use of a matching network system lies in the fact that the impedance of the plasma load is initially unknown. However, there are methods available to approximate this load before testing to aid in the system design. In order to estimate the impedance of an inductively coupled plasma (ICP), a specific type of model can be created. Colpo et al. [18] did so by utilizing the concept of equivalent circuits. An equivalent circuit is an idealized, simple version of an electrically equivalent complex circuit.

L_{Coil} = Antenna Coil Inductance

L_{pl} = Plasma Inductance

R_{pl} = Plasma Resistance

M = Coil and Plasma Mutual Inductance

R_c = Primary Coil Resistance

X_c = Primary Coil Reactance
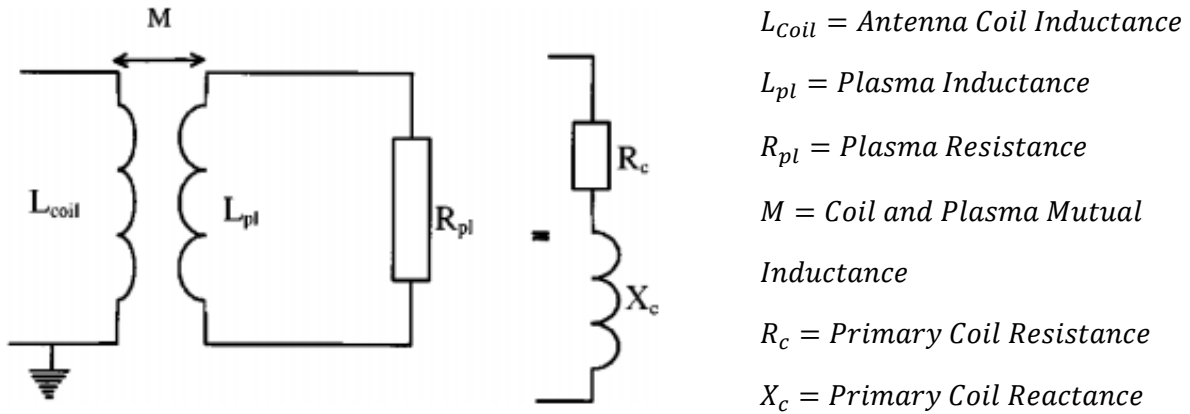
Figure 10. Classical Transformer Model.

The classical transformer model shown in Figure 10 is a simple equivalent circuit that treats the antenna coil as the primary winding of a transformer and the plasma as a resistive secondary winding. With these assumptions, an equation can be derived to estimate the impedance of the primary coil [18].

$$Z_c = \frac{w^2 M^2 R_{pl}}{R_{pl}^2 + w^2 L_{pl}^2} + j\left(wL_{coil} - \frac{w^3 M^2 L_{pl}}{R_{pl}^2 + w^2 L_{pl}^2}\right) = R_c + jX_c \tag{1}$$

In Eq. 1, Z_c represents the impedance of the coil, w represents the frequency of the power source, M represents the mutual inductance, R_{pl} and L_{pl} represent the resistance and inductance of the plasma, respectively, and L_{coil} represents the inductance of the coil.

2.6 Previous MQP Progress

Through research into what other groups have used for RF discharges, it was found that the design of the Pennsylvania State University RFET was the most similar documented example, and reference was made to the published Penn State paper for guidance throughout the project [11]. Following the Penn State example, it was determined that quartz glass would be the ideal material for the thruster's discharge chamber. The properties which contributed to this selection were its low cost and low dielectric losses [19]. For purposes of the 2015 project, gas

was to be introduced to the quartz discharge chamber at a flow rate of 0.75 mg/s. It was decided that the chamber tube would have an inner diameter of 30 mm, a wall thickness of 1.5 mm, and a length of 5 inches. Further research led to the decision to use argon gas, instead of helium (another frequent choice), for its relative safety and low cost.

After finalizing the choice of gas and the dimensions of the quartz chamber tube, MATLAB and COMSOL simulations were used to predict the behavior of the heated gas within the chamber. The MATLAB model estimated performance based on isentropic flow through the throat. From the results, it was decided that the thruster should have a nozzle with an expansion ratio of 50 and a throat diameter of 5mm. However, while the final product had a 5 mm throat, a converging-diverging contour was deemed unnecessary for an initial demonstration and hence not implemented. Next, a CAD model of the discharge chamber was used to create a COMSOL simulation which was used to gather a better understanding of the thruster's thermal behavior. However, the MATLAB and COMSOL thermal models were not completed, and did not fully account for all possible modes of excitation and heat loss. As a result, neutral gas temperatures calculated by the simulation were unrealistically high [1].

Using the results of the MATLAB model, a CAD model was developed to serve as a guideline for the fabrication of the major RFET components. Materials were selected based primarily on their heat tolerances, and the parts were assembled according to the CAD model that had been created. Three 5/16 inch threaded rods were cut to 7 inches in length and used to secure two circular aluminum plates to the ends of the gas chamber. The plates had holes designed to accommodate the threaded rods and both the argon inlet and outlet [1]. The final result of the 2015 RFET team's [1] assembly is shown in Figure 11.
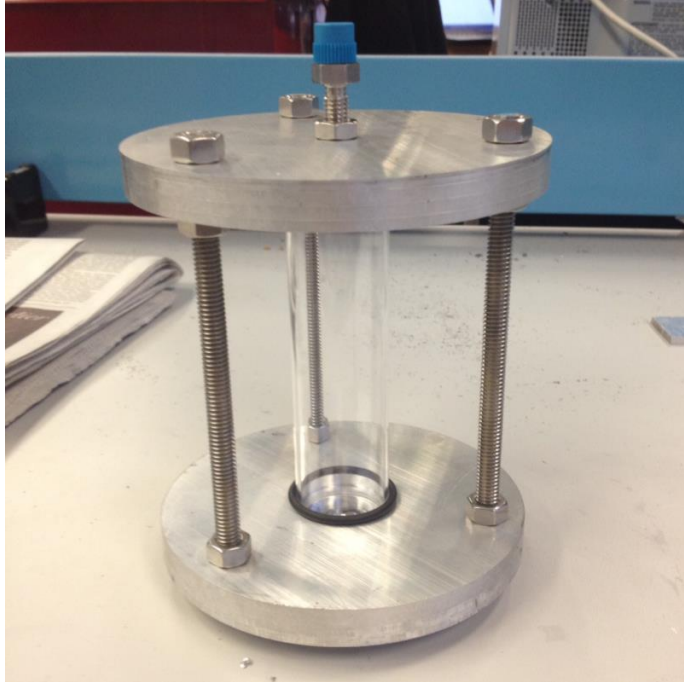
Figure 11. The Previous MQP RFET [1]. The aluminum ends plates are 5.0 inches in diameter.

The T4 chamber was tested and it was found to be in good operating condition. Additionally, a stand for mounting the thruster within the vacuum chamber was designed and most of the parts were purchased for fabrication of both the stand and the matching network [1].

Lastly, the testing facilities were readied. The T4 chamber was prepared for installation of the power source by clearing the necessary space and obtaining the required length of coolant hose for the vacuum chamber and a loaned (from Busek Co. Inc., Natick, MA) type-N feedthrough connector. Finally, the control panel, regulator, and argon tank were all moved over to the T4 chamber to prepare for testing [1].

3. METHODOLOGY

3.1 Thruster Redesign

After a careful review of the design and work completed by the 2015 RFET team [1], it was determined by the 2016 RFET team that the as-built thruster would likely not work due to an oversight in the design of the discharge chamber tube seal system. The intention of the 2015 RFET design was to seat an O-ring in a gap between each end plate and the chamber tube, as shown by the cross-sectional view in Figure 12. The gap was designed to a size such that slight circumferential compression would be exerted upon the O-ring, resulting in the formation of a seal between the ambient vacuum and the discharge chamber.

Figure 12. Cross-section of discharge chamber tube, end-plate seal from 2015 RFET MQP [1].

When project work ended for the 2015 RFET team [1], the diameters of both end plate cavities were not large enough to accommodate the quartz tube and O-rings as planned, leaving the chamber tube unsealed. The discharge chamber tube seal system was redesigned in order to correct the errors from the 2015 design, which were most likely a result of improper machining. This meant performing a complete redesign of the mechanical assembly of the thruster.

In order to avoid the problems encountered by the 2015 RFET team [1], several possible design options were evaluated. Diagrams of alternative seal systems were created, summarizing

the advantages and disadvantages of each. The findings were then presented to the project advisor and lead lab machinist for discussion and selection. Each design option is shown in Figure 13.

Design Option I:
- **Build prior to redesign**
- Cavity diameter not adequate to properly seat O-ring
- No seal achieved

Design Option II:
- **Initially intended design**
- **Pros:**
  - Machining simplicity
- **Cons:**
  - Difficulty with O-ring installation
  - No guarantee O-ring will remain seated when chamber pressurized

Design Option III:
- **New concept, machined groove**
- **Pros:**
  - Guarantees O-ring remains seated
- **Cons:**
  - Undercutting a groove is a more complicated machining process

Design Option IV:
- **New concept, O-ring retainer**
- **Pros:**
  - Guarantees O-ring remains seated
  - Ease of access to O-ring and tube
- **Cons:**
  - System more complex from machining and assembly standpoints

Figure 13. Seal system design options.

After discussion and evaluation of these options, it was decided that an O-ring retainer system, illustrated in Design Option IV, would be ideal. Using SolidWorks, a CAD file of this

Mark I design, shown in Figure 14, was created for both visualization purposes and for reference during the initial lab contact meeting with the lab machinist, Kevin Arruda.
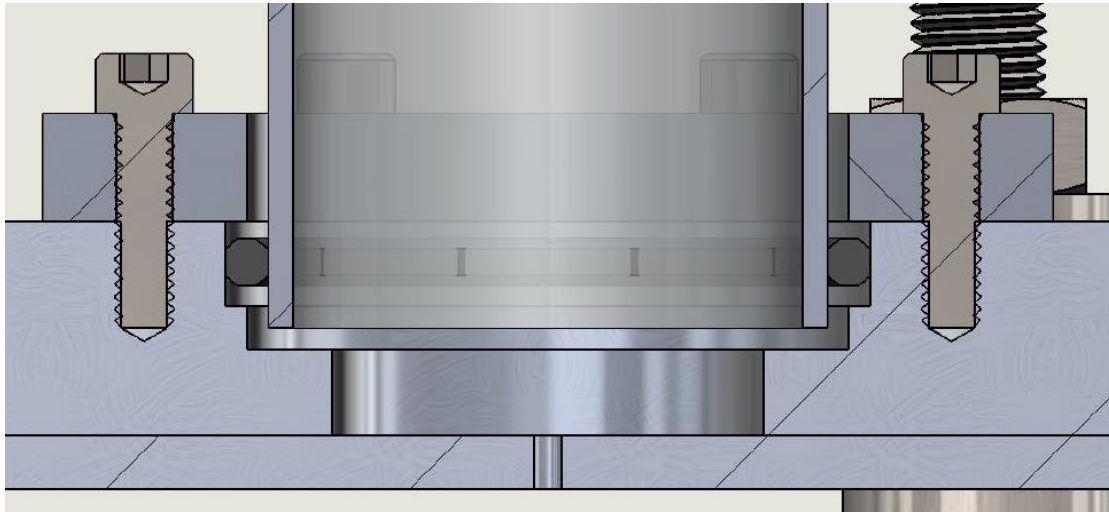
Figure 14. Cross-section of Mark I O-ring retainer seal system.

After continued discussion with the lab machinist and the project advisor, a variant of the O-ring retainer, designated Mark II, was selected as the best option for the project, due to its likelihood of sealing, allowance for easy access to the O-rings and chamber tube, and general adaptability. This new design involved not only retaining the O-rings, but compressing them against the chamber tube using the beveled face of the retainer ring, properly dimensioned for maximum seal according to the Parker O-Ring Handbook [20].

There were a number of additional changes made to the seal system and overall thruster hardware designs from those initially proposed, as a result of conversation with the lab machinist and project advisor. The first of these changes involved the holes for the O-ring retainer fasteners. Rather than tap blind holes in the bottom plate for the fastener bolts, through-holes were chosen in order to eliminate the possibility of trapping air in the bolt cavities when in vacuum, which could result in extended pump down time. A nozzle plate O-ring seal was also included in the Mark II design. This seal would be achieved using a second O-ring, for which a groove was designed to be machined into the nozzle-side of the bottom plate. This additional seal was necessary to prevent propellant from escaping between the bottom and nozzle plates. Such a

seal was not implemented by the 2015 RFET team [1], as a nozzle plate was not included in their design and the exit orifice was machined directly into the bottom plate instead. However, with the prospect of expedited and simplified nozzle alterations in mind, it was decided that incorporating the separate plate into the new design would be optimal.

The addition of a nozzle plate brought with it some complications. Mainly, the supporting threaded rods were precut to a length that could not accommodate the additional 0.25 inches in assembly length resulting from addition of a nozzle plate. However, a larger issue arose upon realization that the previous end plate cavity diameters, while too small for the original O-ring seat design, were too large for the new intended O-ring compression design. The oversized gap between the cavity edge and the chamber tube, indicated by callout 1 in Figure 12, would yield an unreliable seal. Therefore, it was decided that new end plates would have to be machined to the dimensions deemed adequate for the O-ring compression seal system, the finalized version of which is shown in Figure 15.
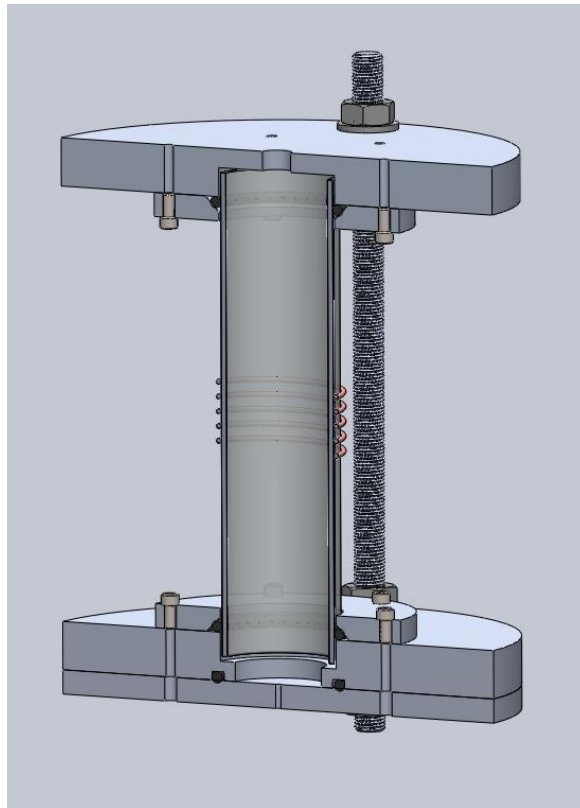
Figure 15. SolidWorks design of the redesigned Mark II thruster assembly.

Once the final design had been approved by both the project advisor and lab machinist, it was required that tutorial courses, offered by the University, on DP Technology's (Camarillo, CA) computer aided manufacturing (CAM) software, ESPRIT, be taken by one of the team members. Once ESPRIT training had been completed, fabrication of the end plates, retainer rings, and nozzle plate began. The 6061 aluminum plates used for these parts, initially 12.0 inches square, were first cut to reasonable sizes (i.e. roughly 6.0 inches square for the end and nozzle plates, and roughly 3.0 inches square for the O-ring retainers) with a vertical band saw. This process created four 6.0 inch squares from the 0.5 inch thick plate (two for the endplates, one for a fixture, and one spare), as well as one 6.0 inch square and two 3.0 inch squares (for the nozzle plate and O-ring retainers, respectively), and plenty of excess from the 0.25 inch thick plate. Following these rough cuts and squaring of the edges with a manual vertical mill, a Haas TM-1 CNC mill was used to drill the holes and mill the central cavities in all plates. The results of these first CNC operations are shown in Figure 16. After these first operations, all holes that required threads were manually tapped, all parts were deburred to ensure level seating on the fixture plate for the next operation, and the squares were cut into rough circles with a vertical band saw. The second CNC operation milled the outer diameter for each part, using the premade fixture plate as shown in Figure 17, and also milled the O-ring groove in the bottom end plate. The sharp edges were then filed, and the sealing surfaces were polished with fine sandpaper.
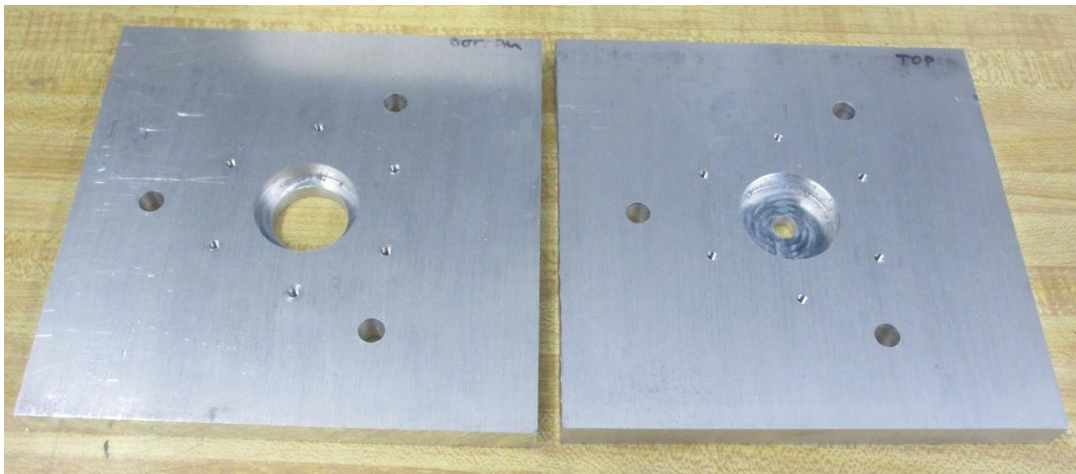
Figure 16. Top and bottom thruster end plates following first CNC operation.
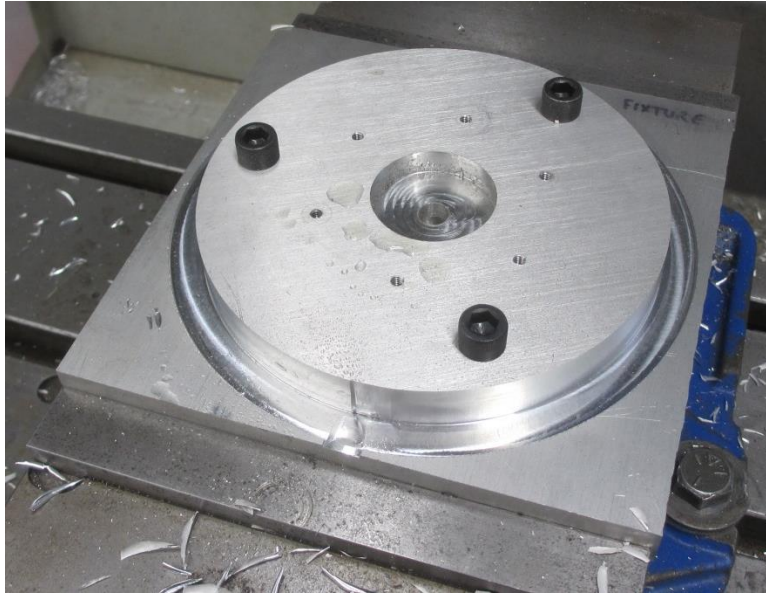
Figure 17. Top plate mounted in fixture, post-operation.

In addition to fabricating these aluminum plates, three new threaded rods were cut to 12.0 inches, which compensated for the addition of the 0.25 inch thick nozzle plate and offered more material to work with for mounting the thruster to the test stand. These rods were quickly and easily cut using a hacksaw, and any burrs or defects were removed from the end threads using a file. Another modification to this design, in comparison to that of the 2015 RFET team [1], was the addition of aluminum tubing around the threaded rod. These three lengths of tube act as spacers to separate the plates at a specified distance from one another with precision, compared to the previous method of manually adjusting nuts on each rod. The tubes were cut to 4.9 inches using a hacksaw, and then more accurately turned to 4.75 inches using a lathe.

While designing and integrating a diverging nozzle was considered, it was decided that this was beyond the scope of this project. Therefore, a simple, constant diameter throat, as originally depicted in Figure 16, was drilled into the nozzle plate. This throat, sized to approximately 1.0 millimeter based on choked flow calculations, would allow for propellant to exit the discharge chamber tube. The individual thruster components are displayed in Figure 18. The completed thruster, shown in Figure 19, was assembled after cleaning all components with alcohol in preparation for integration into the vacuum chamber.
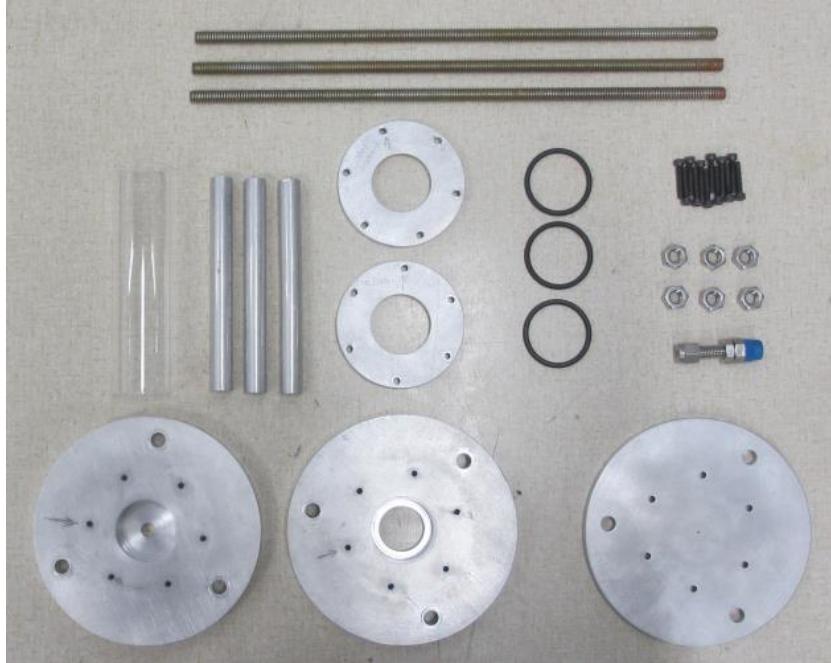
Figure 18. Thruster mechanical assembly components.

Figure 19. Completed thruster mechanical assembly.

3.2 Design and Implementation of Matching Network

The RFET uses an RF power source to send current through an antenna coiled around a chamber containing argon gas. The current-carrying coil delivers power to the load. Since the thruster uses a 600 W (maximum) RF power source operating at 13.56 MHz, an impedance matching network was designed to minimize the power reflected to the source, thereby maximizing the power coupling efficiency to the thruster. The design of the matching network should be such that the impedance between two circuit branches have equal real values of the impedance (resistance) and cancelling imaginary values of the impedance (reactance).

3.2.1 Matching Network Design

Figure 20 shows the conceptual wiring diagram for the electrical components of the RFET. Impedance matching networks consist of inductors and capacitors wired to create a circuit that matches the impedance of the source to the impedance of the load. It was determined by the team that a simple L-type matching network design, which requires only one capacitance value and one inductance value, should be able to match the impedance of this system [21]. In the L-network that was chosen, the capacitor is placed in series with the source and the inductor is placed in parallel with the load (Figure 20).
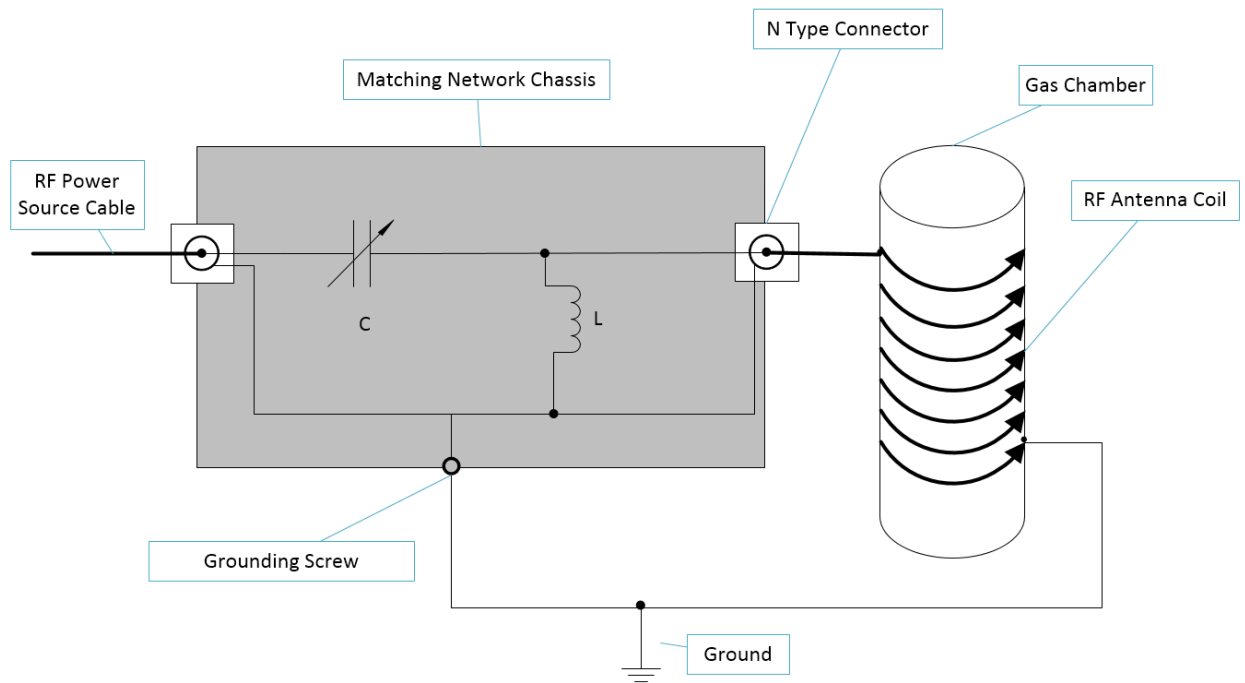
Figure 20. Matching Network Wiring Diagram.

i. Representative Load Characteristics

Since the circuit had to be designed without experimental data for the (plasma) load impedance, sample impedance values were selected from published experimental data [18]. This data considered the resistance and reactance of a plasma discharge, using argon, over a range of RF power and discharge pressure representative of what was expected for the RFET. Figure 21 shows the resistance of argon discharge versus RF power at three different pressure levels, while Figure 22 shows the reactance of argon versus power at the same three pressure levels (from Ref [1] and Ref [18]).
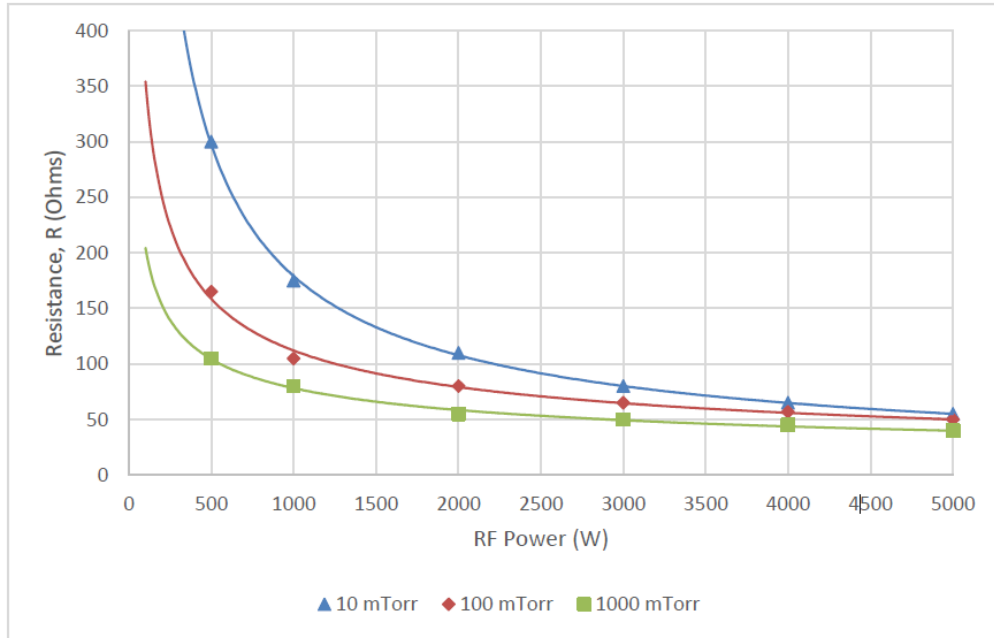
Figure 21. Resistance vs. RF Power for Different Argon Pressures. Plot from Ref. [1] based on data originally published in Ref. [18]. Ref. [1] © 2015 by the authors.
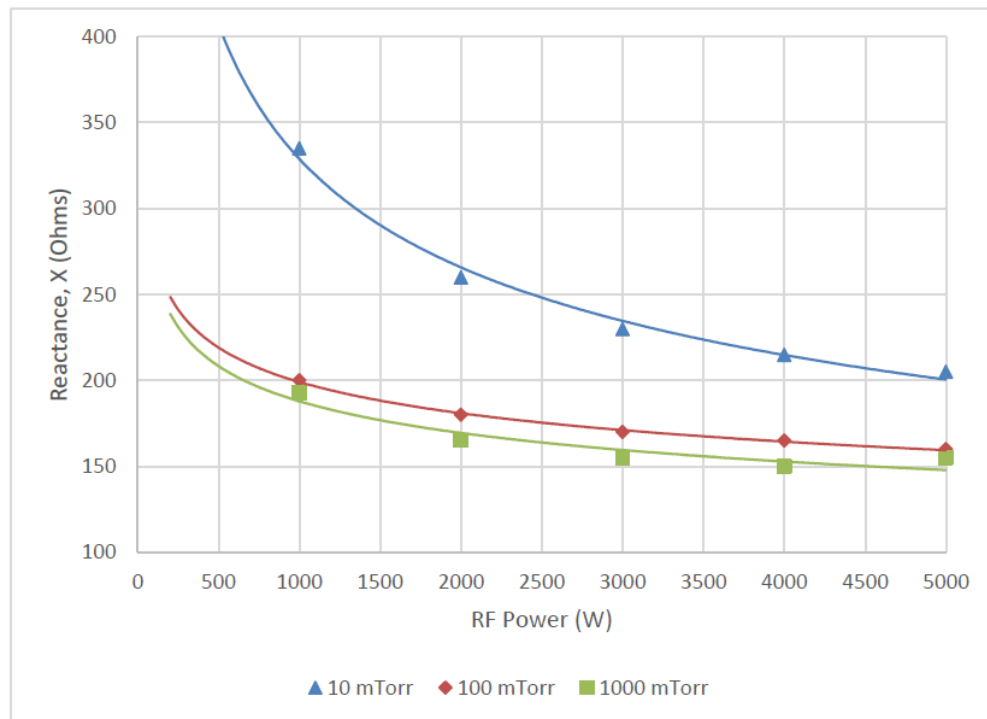
Figure 22. Reactance vs. RF Power for Different Argon Pressures. Plot from Ref. [1] based on data originally published in Ref. [18]. Ref. [1] © 2015 by the authors.

ii. Determining Required Inductance and Capacitance

To determine the impedance of the load under a given set of operating conditions, sections of the circuit are isolated and analyzed from different points in the circuit. Figure 23 shows the circuit sectioned into three groups.
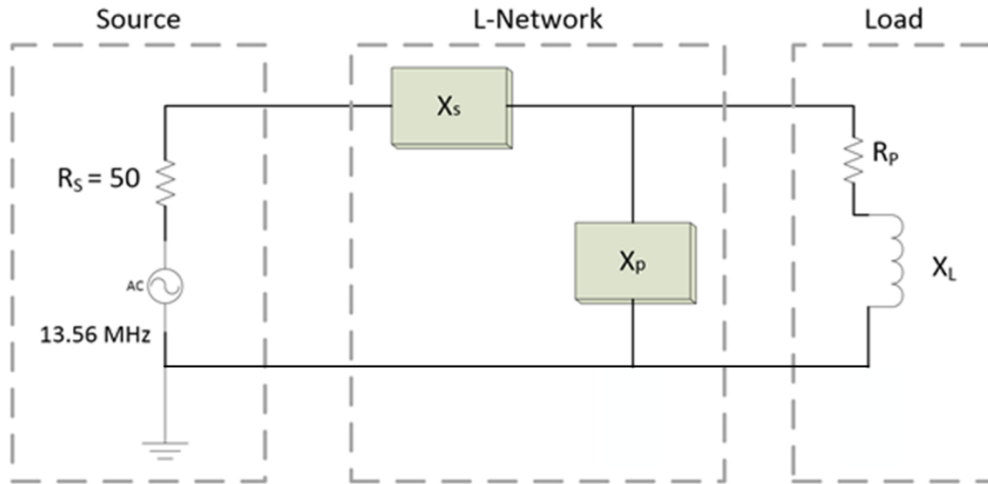
Figure 23. Matching Network Circuit Diagram for Circuit Analysis.

Looking at just the L-Network group connected to the load group, shown in Figure 24, the electrical components in the source group can be ignored. Instead, only the impedance value from the source is considered. Since it is known that the impedance of the RF source is $R_S = 50\Omega$, the overall impedance of the two remaining groups, the L-network and the load, should result in a resistive component of 50Ω and a reactive component of zero.
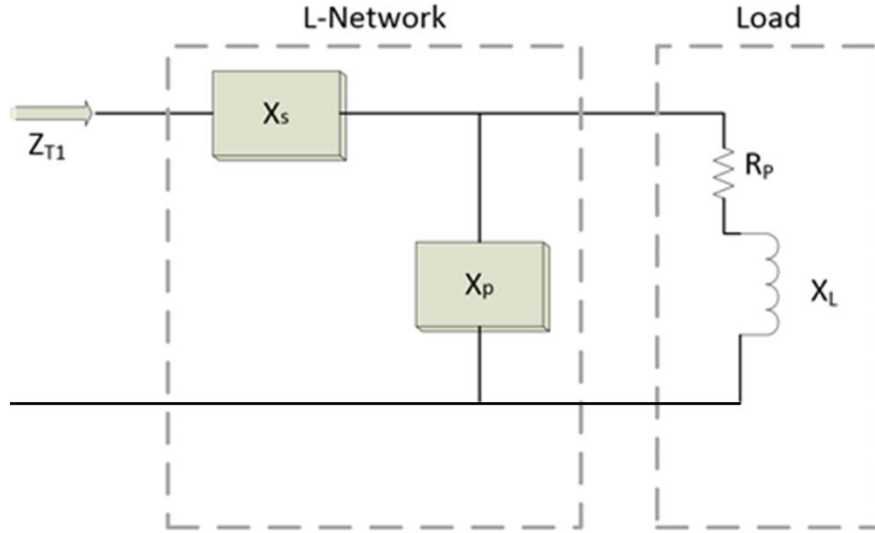
Figure 24. Isolated Circuit Diagram for First Circuit Analysis.

The overall impedance of the L-Network and the load, shown as Z_{T1} in Figure 24, can be found using Eqs. 2-6 from Ref [22]

$$Z_1 = 0 + X_s j \qquad (2)$$

$$Z_2 = 0 + X_p j \qquad (3)$$

$$Z_3 = R_L + X_L j \qquad (4)$$

$$Z_4 = \frac{(Z_2 Z_3)}{(Z_2 + Z_3)} \qquad (5)$$

$$Z_{T1} = Z_1 + Z_4 \qquad (6)$$

where Z_1 is the impedance of the series component within the matching network, Z_2 is the impedance of the parallel component within the matching network, and Z_3 is the impedance of the load. Z_4 is the equivalent impedance value of the two parallel branches in the circuit. Lastly, Z_{T1}, which is the total impedance for the circuit of this method, is the equivalent impedance value for the component in series and the newly resolved Z_4 impedance. The total impedance is set equal to $Z_{T1} = 50 + 0j$, since the combined impedance from the L-Network and the load must match the real impedance from the source and cancel the imaginary impedance from the source. X_S and X_P are unknown values that are solved for by matching the real and imaginary

36

components. Once X_S and X_P are found, the values for inductance (L) and capacitance (C) can be calculated by using Eq. 7 and Eq. 8, which are the standard relationships for inductive and capacitive reactance:

$$L = \frac{X_P}{2\pi f} \tag{7}$$

$$C = \frac{1}{2\pi f X_S} \tag{8}$$

Determining X_S and X_P requires solving two simultaneous, non-linear equations, one from matching the real component, and one from matching the imaginary component. A MATLAB script (see Appendix A and B) written by the project advisor, Professor Blandino, was used to solve these equations and return values for X_S, X_P, Rm_{ZT} (the real component of the source impedance), Im_{ZT} (the imaginary component of the source impedance), C, and L. The values calculated by using this circuit analysis method are as follows:

$$X_S = -143.61 \ \Omega \qquad Re_{zt} = 50 \ \Omega \qquad C = 81.73 \ pF$$

$$X_P = 308.89 \ \Omega \qquad Im_{zt} = 0 \ (\sim 10^{-10}) \ \Omega \qquad L = 3.63 \ \mu H$$

The real and imaginary components of the source impedance (50+0j) were returned as expected, which provided a measure of confidence in the method.

As an additional check of these results, the analysis can be repeated from a different point in the circuit. For this circuit analysis, the L-Network group connected to the source group was isolated "as seen" by the electrical components in the load group, as shown in Figure 25.
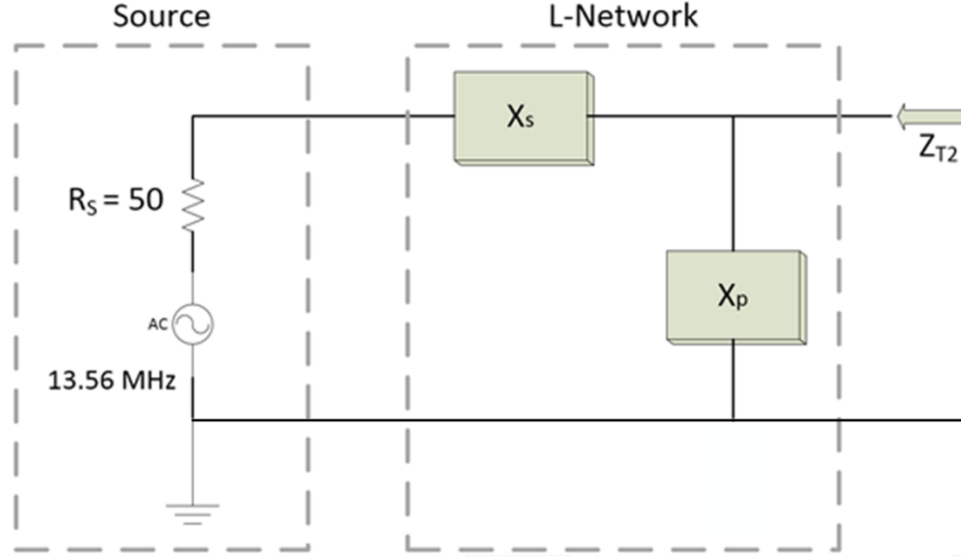
Figure 25. Isolated Circuit Diagram for Second Circuit Analysis.

Using the data obtained from Figure 21 and Figure 22, the impedance of the load for the sample operating point is (160 + 220j Ω). Therefore, the overall source and L-Network impedance should equal $Z_{T2} = 160 - 220j$ in order to match the resistive component and cancel the reactive component of the load.

For this circuit configuration, shown in Figure 25, the overall impedance of the source and L-Network groups can be found using Eqs. 9-11 [22],

$$Z_5 = R_s + X_s j \tag{9}$$

$$Z_6 = 0 + X_p j \tag{10}$$

$$Z_{T2} = \frac{(Z_5 Z_6)}{(Z_5 + Z_6)} \tag{11}$$

where Z_5 is the equivalent impedance of the resistance of the power source and the series component within the matching network, Z_6 is the impedance of the parallel component within the matching network, and Z_{T2}, the total impedance for this circuit analysis, is the equivalent impedance value for the parallel component within the matching network and the newly resolved Z_5 impedance. Z_{T2} is set equal to (160 - 220j Ω), since that is the impedance from the load that

must be matched. Again, X_S and X_P are unknown variables that are solved for, and the values for L and C can be calculated using Eq. 7 and Eq. 8

As in the first circuit analysis, a MATLAB script (see Appendix C and D) was written to solve for X_S and X_P, and then calculate the values for Rm_{ZT}, Im_{ZT}, C, and L. The solution generated the exact same results as found in the first circuit analysis:

$$X_S = -143.61 \ \Omega \qquad Re_{zt} = 160.0 \ \Omega \qquad L = 3.63 \ \mu H$$

$$X_P = 308.89 \ \Omega \qquad Im_{zt} = -220.0 \ \Omega \qquad C = 81.73 \ pF$$

3.2.2 Component Selection

Since the thruster will be tested under a range of operating conditions, the load reactance and resistance values, spanning nine test cases varying in chamber pressure and supplied power, were obtained from Figure 21 and Figure 22. The MATLAB script was run using each of those reactance and resistance values to calculate the appropriate capacitance and inductance needed to properly match the impedance for that test case. This resulted in a range of capacitance and inductance values required to match the network over the span of operating conditions for the RFET. Table 2 shows the power input, chamber pressure, reactance, resistance, required capacitance, and required inductance for each case.

Table 2. Matching Network Characteristics Under Varying Operating Conditions

Operating Conditions:	Case A	Case B	Case C	Case D	Case E	Case F	Case G	Case H	Case I
Power (W)		400			500			600	
Pressure (mTorr)	10	100	1000	10	100	1000	10	100	1000
Reactance (Ω)	450	235	220	400	220	210	380	215	202
Resistance (Ω)	400	200	120	300	160	100	265	145	95
Required C (pF)	56.73	80.41	76.29	59.31	81.73	74.91	60.21	81.60	76.20
Required L (µH)	3.53	3.20	4.94	3.73	3.63	6.14	3.86	3.90	6.45

Note: All load resistance and reactance values are from Ref [1] (adapted from Ref [18]) for a representative plasma discharge.

Based on the data presented in the table, the required range of inductance is 3.20 µH to 6.45 µH, and the required range of capacitance is 56.73 pF to 81.73 pF. These values enable proper matching of the thruster's impedance over a range of potential operating conditions. The decision was made to use a variable capacitor and a selection of several fixed inductors which could be arranged such that they are equal to the necessary inductance depending on the desired operating conditions. To account for error and accommodate the wide range of impedance, a tunable capacitor with a range of 16-101 pF was selected. The capacitor has an air dielectric but will be operated in a vacuum. Since the dielectric constant of air and a vacuum are nearly equivalent (1.001 and 1.0, respectively) the capacitor will still perform as expected when placed in the vacuum chamber [19].

Additionally, twelve 3.0 µH inductors were purchased to cover the range of inductance required. The inductors can be switched out of the matching network and rearranged as testing progresses and operating conditions vary. Since this system is operating on a high frequency power supply, the electrical components must be rated for high voltage and high amperage capacities. Therefore, the capacitor has an air dielectric and is rated to handle 4.5 kV. Likewise, the inductors are rated to handle up to 21 A. Tin/silver (lead-free) solder was also purchased, to account for the high temperatures expected within the vacuum chamber, and to eliminate vapor pressure concerns with use of lead-based solder (see Appendix F for item breakdown).

3.2.3 Building the Matching Network

The overall design for the matching network involved constructing the circuit inside of an aluminum enclosure, the chassis, which was then mounted inside the vacuum chamber. A specific value of the inductor was chosen based on the anticipated operating condition, with tuning performed by adjusting the capacitance once the discharge had been initiated. Since the components are inside the vacuum chamber, the capacitor was tuned by using an externally controlled, reversible DC motor. A high torque, low rpm motor was fixed to the outside of the aluminum chassis with the shaft connecting to the variable capacitor through a hole drilled in the chassis wall. The selected motor operated at 6V and was capable of producing a torque of 0.367 N-m with a speed of 2 rpm at maximum power output [23]. A flexible rubber coupler was used inside the chassis to connect the motor shaft to the capacitor. The diameter of the motor shaft was found to be 0.28 inches, while the capacitor shaft was found to be just under 0.25 inches.

Using these dimensions, the decision was made to purchase an Over-Torque-Prevention Vibration-Damping Coupling from McMaster-Carr, which was designed for a 0.25 in. shaft at one end and a 5/16 in. (0.3125 in.) shaft at the other end [24].

The variable capacitor has a structure which is also tied to the set of electrode plates and is therefore grounded if fastened directly to the chassis. For this reason, the capacitor was installed such that the body was isolated (electrically floating) with respect to the enclosure. A PTFE (Teflon) plate, washers, and screws were used to isolate the capacitor and to fasten it to the bottom of the housing box, preventing any electrical connection between the capacitor and the grounded chassis.

A lid for the matching network chassis was fabricated in order to protect the matching network components during testing and to fully enclose the circuit in a grounded structure. This lid, cut from a sheet of 0.03125 inch thick perforated aluminum, was fastened to the open face of the enclosure using sheet metal screws. Once all electrical components had been properly incorporated within the chassis, a hole was drilled in the lid for the antenna to pass through, allowing for connection to the matching network circuit. The hole was placed in such a way to minimize the length of the transmission line to the antenna. The completed matching network enclosure, with lid, is shown in Figure 26.
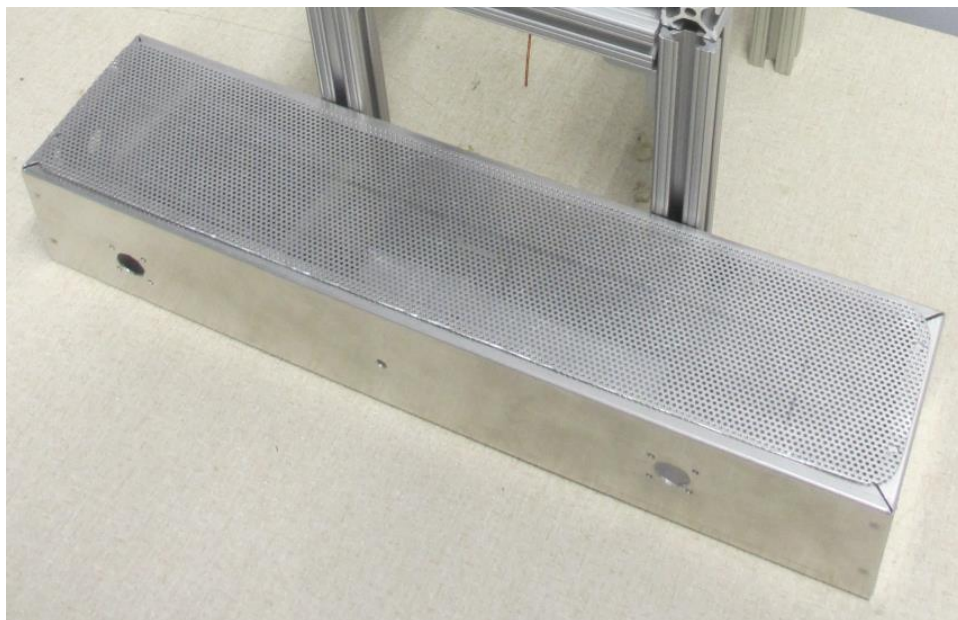
Figure 26. Matching network enclosure assembly, without lid fasteners in place.

3.2.4 Circuit Construction

Twelve (12) AWG silver plated copper wire was soldered to the center conductor of the RG65 coaxial cable running from the RF power supply, using the lead-free solder. The wire was then threaded through a hole in the matching network chassis and soldered to the positive terminal of the capacitor. From the negative terminal, the silver/copper wire was soldered to one end of the inductor arrangement. As previously mentioned, the group of 3.0 µH inductors was arranged to approximate the required inductance value. These inductors were soldered together using the lead-free solder. From the same end of the inductor arrangement, the silver/copper wire runs through the top of the matching network chassis to reach the antenna coil, creating an electrical node (Node D in Figure 27). The wire was connected to the antenna lead using a Be/Cu inline barrel connector. The antenna was then wrapped around the quartz gas discharge chamber tube, and the opposite lead was again connected to silver/copper wire via barrel connector. This wire was fed back through the hole in the top of the matching network and connected to the other end of the inductor arrangement, creating Node E (see Figure 27). This effectively placed the load (i.e. antenna coil) in parallel with the inductors while leaving the capacitor in series with the power source. From Node E, the wire was fed out of the matching network through a hole in a side wall of the chassis. The wire was then soldered to the outer braid of the coax cable, which returns to the power source. All electrical connections made during matching network construction were secured with the tin/silver solder, with the exception of the antenna leads. A separate silver/copper wire was soldered to a grounding screw, which was fastened to the side of the matching network, and connected the chassis to a grounding strap within the vacuum chamber. Refer to Figure 27 for the system schematic and Figures 28 and 29 for the physical assembly.
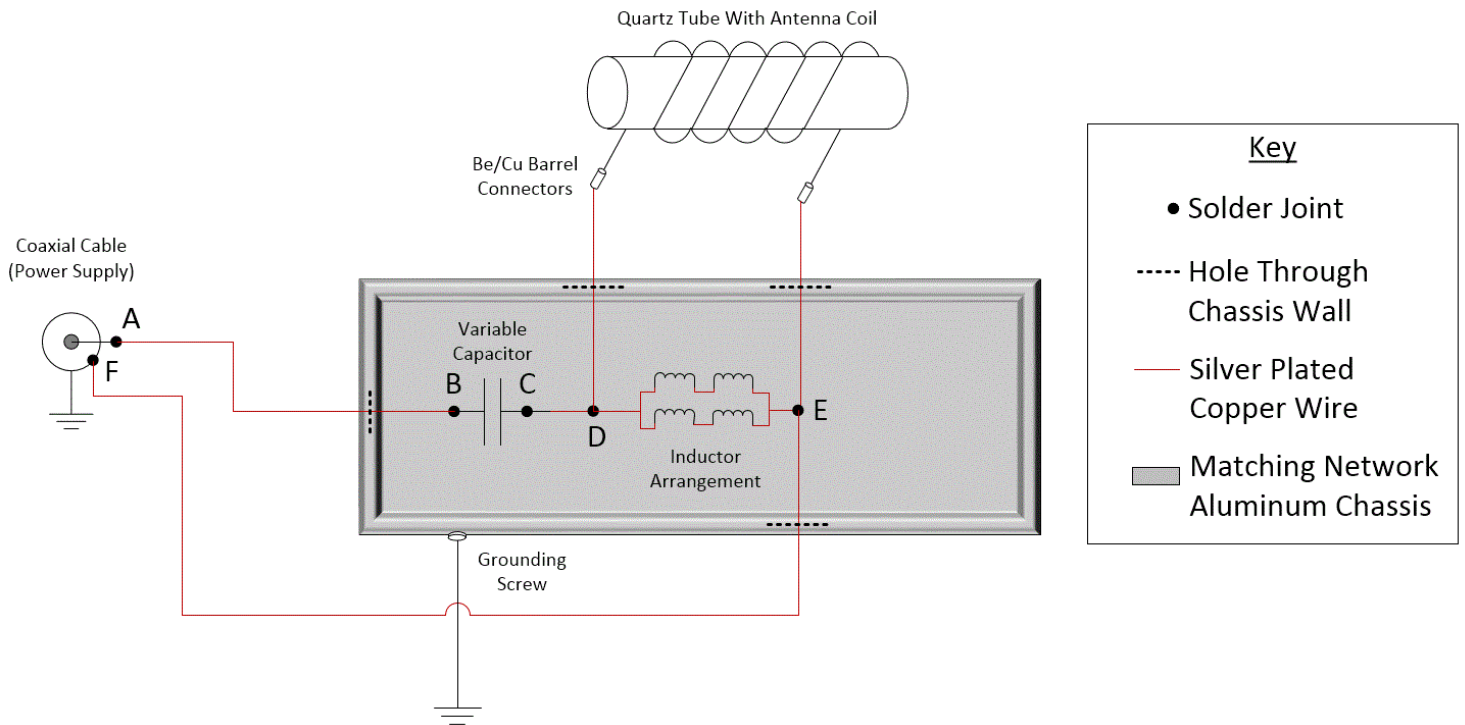
Figure 27. Matching Network Wiring Schematic.
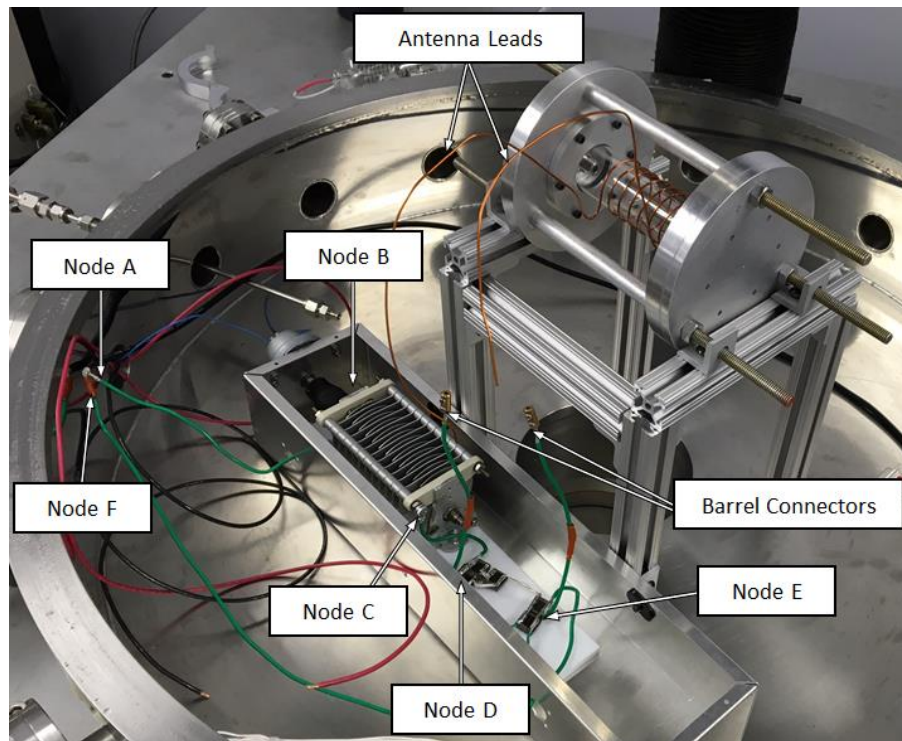
Figure 28. Integration of thruster, stand, and matching network within vacuum chamber base with electrical node callouts.
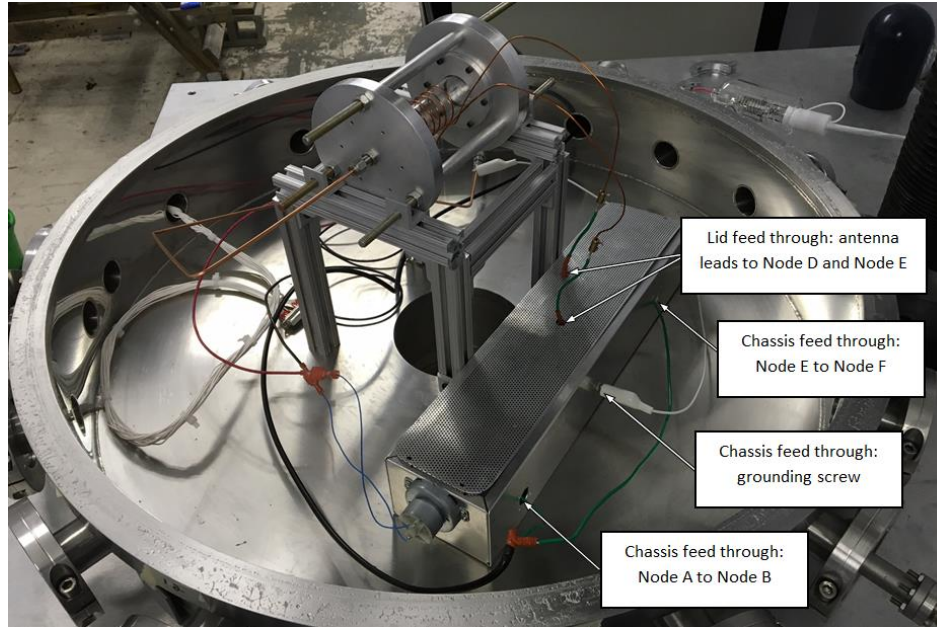
Figure 29. Integration of thruster, stand, and matching network within vacuum chamber base with matching network chassis feedthrough callouts.

3.3 Design and Construction of RF Antenna

When constructing the coil, one of the most critical aspects was the determination of the turn count. As shown previously in Eq. 1, the inductance is a large factor in determining the coil specific impedance. Since the matching network is based on the plasma load impedance, it is beneficial to keep the inductance as low as possible, which can be done by lowering the turn count. As discussed in Section 2.5, it was suggested by Dr. Lynn Olson of Busek Co. Inc, that the coil count for the RF antenna be approximately 4 to 5 turns. However, the turn count also needs to be high enough to keep the wire transmission current below the maximum allowed value in order to prevent damage to the coil. Using this suggestion along with the minimum and maximum matching network inductance values (found in Section 3.2.2), a design for the RF antenna was created using the following formulas to approximate coil inductance [25].

$$L = \frac{N^2 \mu A}{l} \qquad (12)$$

Where L is the inductance of the coil (in units of Henries), N is the number of turns in the wire, and l is the length of the wound coil in meters. Due to expansion, the length of the coil was set to one half of the discharge chamber length at 0.062 m. Additionally,

$$\mu = \mu_r \mu_o \qquad (13)$$

where μ is the absolute magnetic permeability of the core material, μ_r is the relative permeability (set to 1.000513, in our case), and μ_o is the permeability of free space, set to $(1.26e^{-6}) \left[\frac{T-m}{A} \right]$. Lastly, A is area of the circle formed by the coil in square meters. With the diamter of the discharge tube and the thickness of the wire, the total coil radius is 0.017125 m and the area is 0.00092 m. Using a turn number of $N=7$ gives an inductance value of $L = 9.12 \ \mu H$.

The value for the impedance using a turn number of $N=7$ at 500 W and 100 mTorr and a frequency of 13.56 MHz is 49.54 Ω. This result is valid only for a specific power and pressure environment. After using Eq. 1 to find the primary coil resistance, it was determined that the resulting current is below the 16 AWG maximum of 3.7 amperes.

Since the outer diameter of the gas chamber is 33 mm, the copper wire for the antenna was tightly wrapped around a dowel with a diameter of 30 mm. This was done to ensure that after the wire was removed from the dowel and the coil expanded, it would still fit tight to the outer diameter of the quartz discharge chamber tube in order to prevent slippage along the tube.

3.4 Test Facilities and Systems

Testing was carried out in the WPI Vacuum Test Facility's (VTF) Tank 4 (T4). The power source used was an ENI model OEM-650A RF plasma generator, shown in Figure 30. In order to regulate gas flow, a flow control panel, shown in Figure 31, was installed on an electronics rack near the T4 testing chamber. A regulator and an argon tank were also placed next to the T4 chamber. A feedthrough was purchased by the 2015 RFET team [1] in order to permit gas flow into the vacuum chamber, through the chamber wall. Since argon gas is potentially harmful when exhausted into a closed area (i.e. if it displaces too much oxygen), an exhaust flow system was devised by the 2015 RFET team [1] as well. A rubber hose adapter was

attached to the output of the T4 chamber mechanical pump, allowing for exhaust to be directed outdoors through the loading bay door of the VTF [1].

Figure 30. ENI OEM-650A RF Power Supply [1].

Figure 31. Instrument Panel Showing Flow Control Panel and Argon Tank In Final Location [1].

The system of pumps located underneath the T4 chamber serve to create and maintain a vacuum environment required for operation of the thruster. The three pumps can operate in succession, if required. The first pump is a Leybold Trivac D16B; a rotary-vane dual-stage

mechanical pump that serves as a roughing pump, incrementally lowering the pressure to at least 0.1 Torr [26]. Once this pressure has been achieved, a Leybold Turbovac 361 turbomolecular pump is turned on, which further decreases the chamber pressure. If vibration due to operating the turbomolecular pump becomes an issue for a particular experiment, the final pump, a Physical Electronics 640 I/s Ion Pump, can be turned on at pressures less than 0.001 Torr. Due to the irrelevance of vibrations on RFET testing, there was no plan to use the third pump during tests [1]. With the pumps operating, the chamber pressure corresponding to anticipated flow rates should be at or below 0.001 Torr, creating a satisfactory pressure ratio across the nozzle throat to insure the flow is choked. The discharge chamber pressure is anticipated to vary from 0.0173 to 0.6918 Torr, depending on the flow rate.

In order to measure the vacuum chamber pressure, several gauges are installed in the vacuum apparatus. Gauges denoted as G1 and G2 in Figure 32 are Thermovac T221 thermocouple gauges, which measure pressure based on the thermal conductivity of the residual gas. The third gauge, denoted G4, is a Varian Agilent Model 572 Ionization gauge, which can be utilized only at pressures below 0.001 Torr.
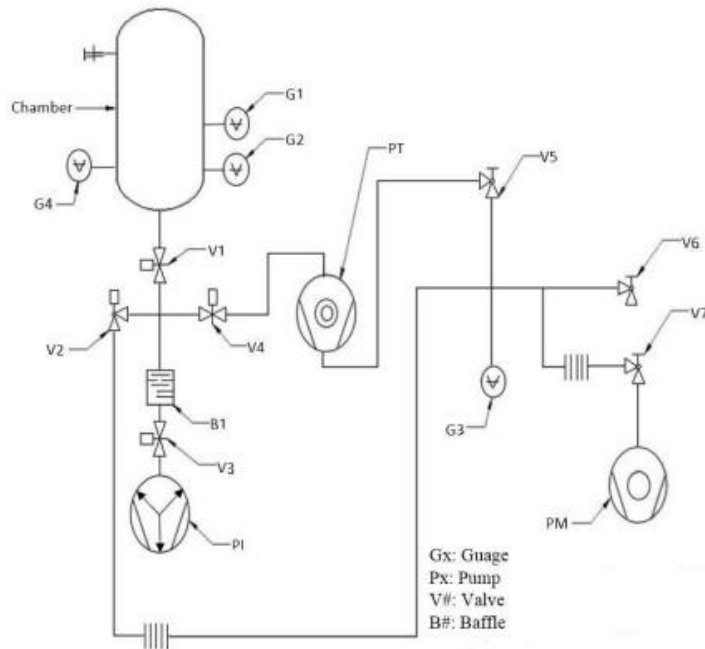
Figure 32. Schematic of T4 Vacuum System [1].

3.5 System Testing

3.5.1 Facility Preparation

Tests of the T4 vacuum chamber were required, in order to ensure that it was still in operating condition and able to sustain a vacuum for an extended period. The first of these tests was the rate-of-rise (ROR) test that served as a chamber leak detection test. The chamber was pumped down using the modified procedure developed by Gonzalez et al. [27]. The chamber, initially at 2.5 Torr, was pumped down to 16 mTorr and the ROR procedure was followed as instructed. Two separate tests were performed to ensure an accurate rate-of-rise recording. The first test took place over 15 minutes at 2.5 minute intervals, while the second test took place over five minutes, at one minute intervals. Table 3 shows the pressure values of the main valve (G1) and foreline (G3) as well as the resulting rate-of-rise for the first interval. Table 4 shows the results for the second interval.

Table 3. Rate of Rise Test Interval #1 [11/20/2015].

Time (s)	Chamber Pressure (mTorr)	Chamber Rate of Rise (mTorr/min)	Foreline Pressure (mTorr)	Foreline Rate of Rise (mTorr/min)
0	17		7.6	
150	17	0	8.8	0.48
300	18	0.4	9.8	0.4
450	18	0	10	0.08
600	18	0	11	0.4
750	18	0	12	0.4
900	18	0	12	0

Table 4. Rate of Rise Test Interval #2 [11/20/2015].

Time(s)	Flange 15 Pressure (mTorr)	Foreline Pressure (mTorr)
0	74	42
60	74	42
120	74	42
180	74	42
240	74	42
300	74	43

The average rate-of-rise was found to be 0.07 mTorr/min, well below the upper limit of 5 mTorr/min. This value indicated that the integrity of the chamber was suitable for experimentation. All data was recorded in the T-4 experimental log book.

3.5.2 Flow Calibration

When designing the system for gas operations in applications such as the RFET, calibrating the flow rate is a critical step. Several types of mass flow meters are available for use in measuring these flow rates within an uncertainty specified by the manufacturer of the controller. However, these controllers need to be recalibrated periodically. A Bubble-o-Meter ™ brand bubble meter was utilized for flow calibration of the argon gas being introduced into the vacuum chamber (see Ref [31] and Ref [32]).
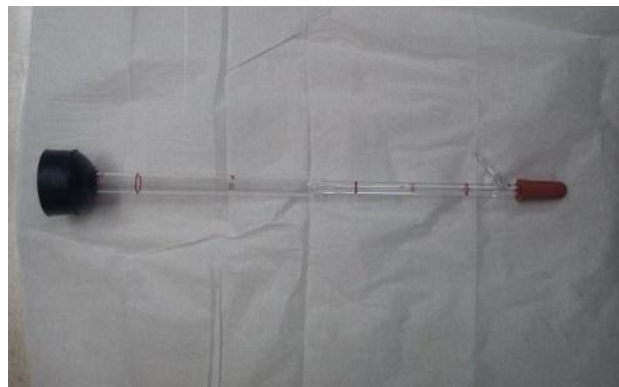
Figure 33. Bubble-o-Meter™

As pictured in Figure 33, the bubble meter was marked with two different volume levels for use a variety of values of mass flow rates. With a set flow rate, a bubble travels through the apparatus. The flow rate is determined by the time it takes the bubble meniscus to travel over a set distance. Using different flow rates and referring to Ref [33], the flow calibration test was conducted and data was recorded (see Figure 34).
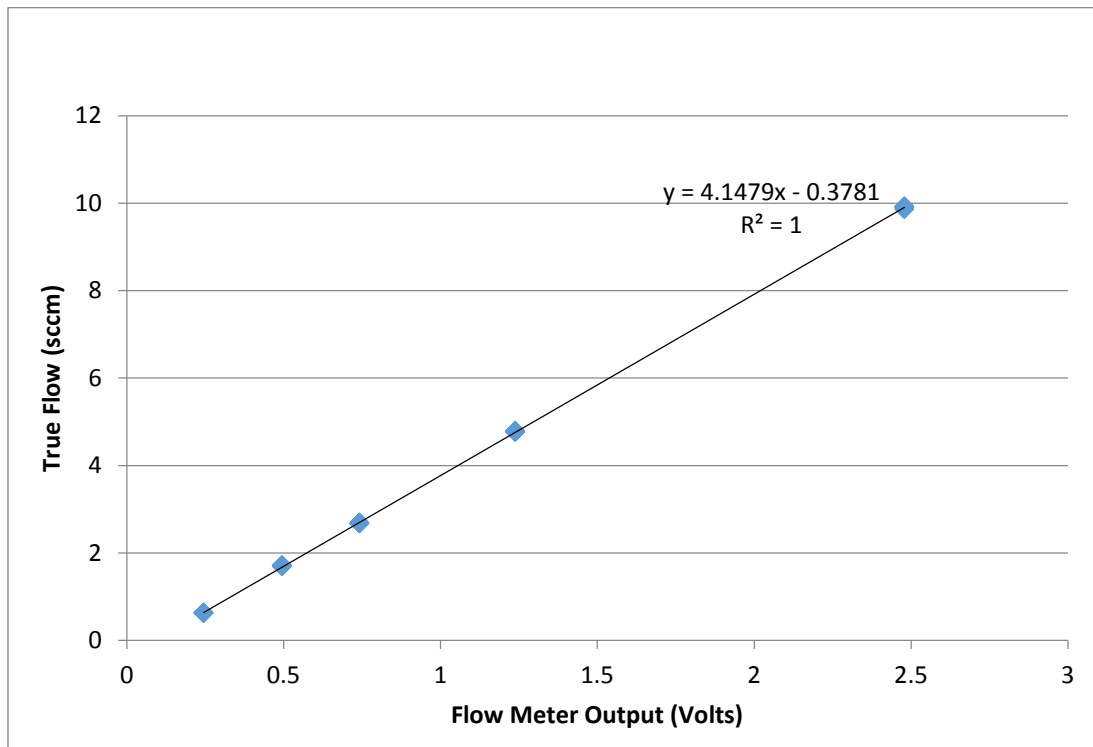
Figure 34. Bubble Meter Flow Calibration Results.

As the linear fit in Figure 34 shows, the mass flow meter operated predictably with an acceptable range of uncertainty. Additionally, the equation from the curve fit was used in the LabVIEW virtual instrument (VI) to convert the raw flow meter output (in volts) to actual units of standard cubic centimeters per minute (sccm) for display to the operator.

i. Low Pressure Flow Characterization

In order to achieve pressures lower than 0.1 Torr in the vacuum chamber, the turbomolecular pump needed to be activated. Prior to final testing, a test which served to characterize the chamber pressure behavior at low torr values in response to various argon gas

flow rates, in standard cubic centimeters per minute (sccm) was conducted. The procedure detailing the activation of the turbopump can be found in Ref. 27.
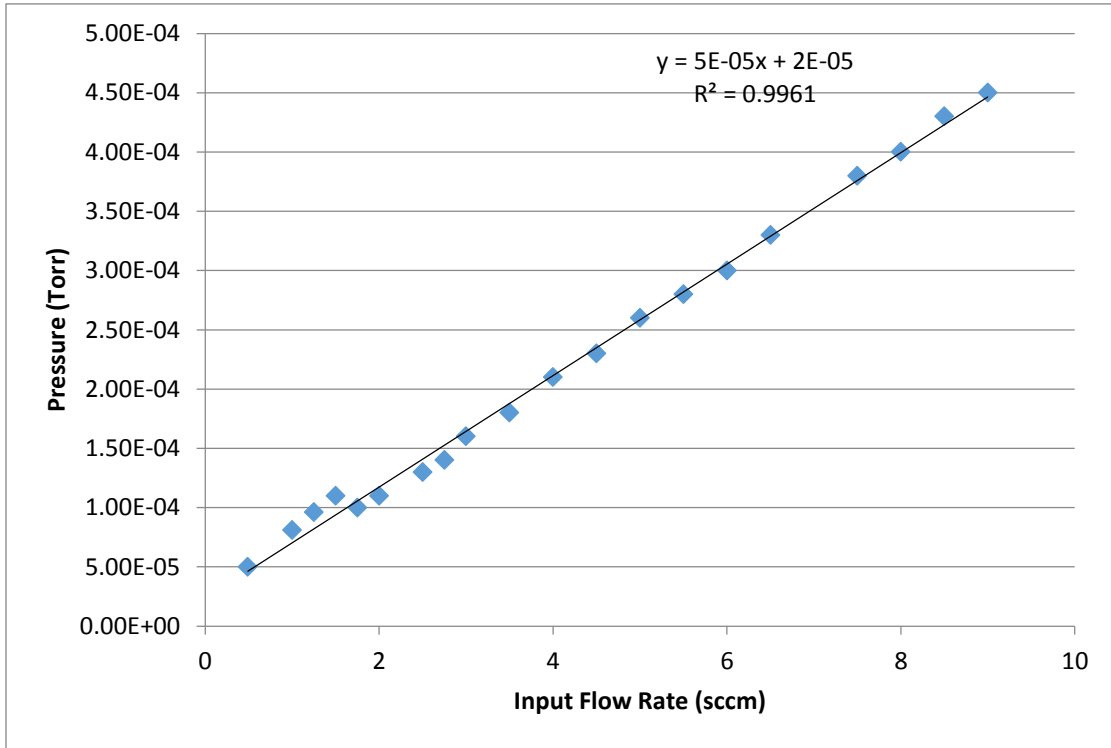
Figure 35. Chamber Pressure vs. Flow Rate Characterization.

As shown in Figure 35, the pressure increases linearly with respect to increasing flow rate. This test confirmed that the pumping facility would be able to maintain a background pressure in the low 0.1 mTorr range over the range of flow rates anticipated for the RFET testing (0.5 – 2.0 sccm).

ii. Chamber Electrical Isolation

While inspecting the chamber, it was found that the flanges for the power feedthrough were not electrically isolated from the chamber. From a safety standpoint, it would be preferable to have the chamber electrically isolated from outer conductor of the type-N RF power cable. Unfortunately, the project inventory did not possess the parts necessary to isolate the chamber

completely. Additionally, the cost of ordering an isolating feedthrough connection was prohibitive. One alternative considered was to manufacture the required part. Using the K.J. Lesker Company sample solid model for a type QF, "full nipple" flange as a baseline, a modified version was created in SolidWorks to meet the isolation needs (Figure 36).
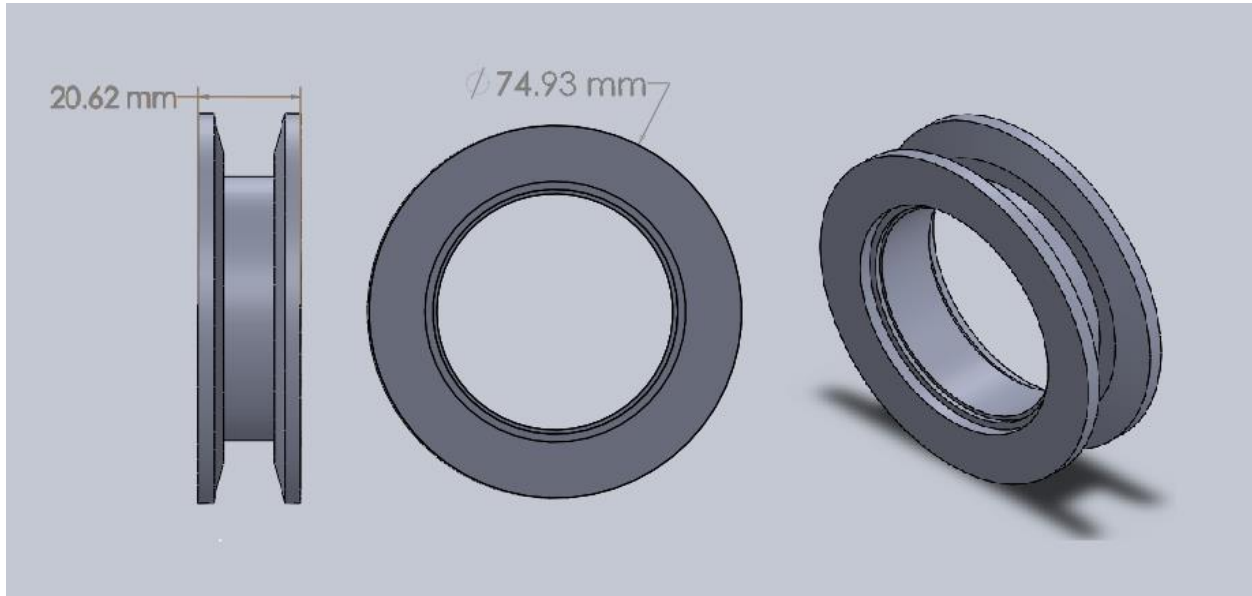
Figure 36. Vacuum Chamber Electrical Isolation Flange.

A key factor in determining design and manufacturing specifications was the time remaining for completion of the project. In consideration of this limitation, it was decided to manufacture the part using 3-D printing technology. Using a plastic printed part was not a perfect solution, however. Two main concerns were brittleness and porosity of the part. In order to compensate for the brittleness, the length of the flange was chosen to be as short as possible while still allowing clearance for the surrounding clamps. To decrease effects of the porosity, the faces of the interior of the part were coated with a spray polyurethane sealant and left to cure.

A rate-of-rise test with the installed 3-D printed part was conducted in order to ensure the vacuum chamber functioned properly with it. This test enabled determination of whether or not leakage was introduced with addition of the plastic component. Unfortunately, a significant leak was present as a result of the part installation. The test was halted in order to investigate. The part was apparently being deformed by the metal centering ring that supports the O-ring, due to

the pressure differential. This was possibly introducing additional leak points, which would account for the leak. After consideration, it was decided to apply a spray-on rubber sealant around the outer tube and inward facing rings (exterior surface only). The test was conducted once more and seemed to hold up better than before. Unfortunately, at around 400 mTorr, it became apparent that there was still a leak. For the purposes of the test, the 3-D isolation part was eliminated from our design and the decision made to use the existing type-N feedthrough. To insure safe operation, the entire vacuum chamber would be carefully grounded to the grounding point in the laboratory (through the ground terminal in an outlet receptacle).

3.5.3 Discharge Chamber Tube Pressure Analysis

In preparation for vacuum testing, an Excel tool was developed to generate plots of discharge chamber tube pressure versus flow rate at a range of operating temperatures. These plots were then used to estimate what flow rate would yield a particular discharge chamber pressure, allowing for better understanding of the test conditions.

Since the back pressure during testing was to be sustained at vacuum levels, on the order of $0.05 - 0.5$ millitorr, the flow would be continuously choked at the throat of the thruster. This known condition allowed for flow rate and chamber pressure to be related using the choked flow equation, Eq. 14 [34]. A rearranged form of this equation, given by Eq. 15, was then used to calculate and tabulate multiple columns of data, each representative of a defined operating temperature. Each row within this table of data corresponded to a different flow rate. In this equation, P_C refers to the pressure within the discharge chamber, $\dot{m}$ is the injected propellant mass flow rate, T_C is the temperature within the discharge chamber, R is the specific gas constant (208 J/kg-K for argon gas), and γ is the specific heat ratio (1.66 for argon gas).

$$\dot{m} = \frac{AP_t}{\sqrt{T_t}} \sqrt{\frac{\gamma}{R}} \left(\frac{\gamma+1}{2}\right)^{-\frac{\gamma+1}{2(\gamma-1)}} \tag{14}$$

$$P_C = \frac{\dot{m}}{A_t} \sqrt{\frac{T_C R}{\gamma} \left(\frac{\gamma+1}{2}\right)^{\frac{\gamma+1}{\gamma-1}}} \tag{15}$$

These columns of data were then plotted in Excel, yielding Figure 37 (for a particular set of discharge chamber temperatures, specified in the accompanied legend), which was used for pre-test estimation and analysis of the expected discharge chamber conditions.
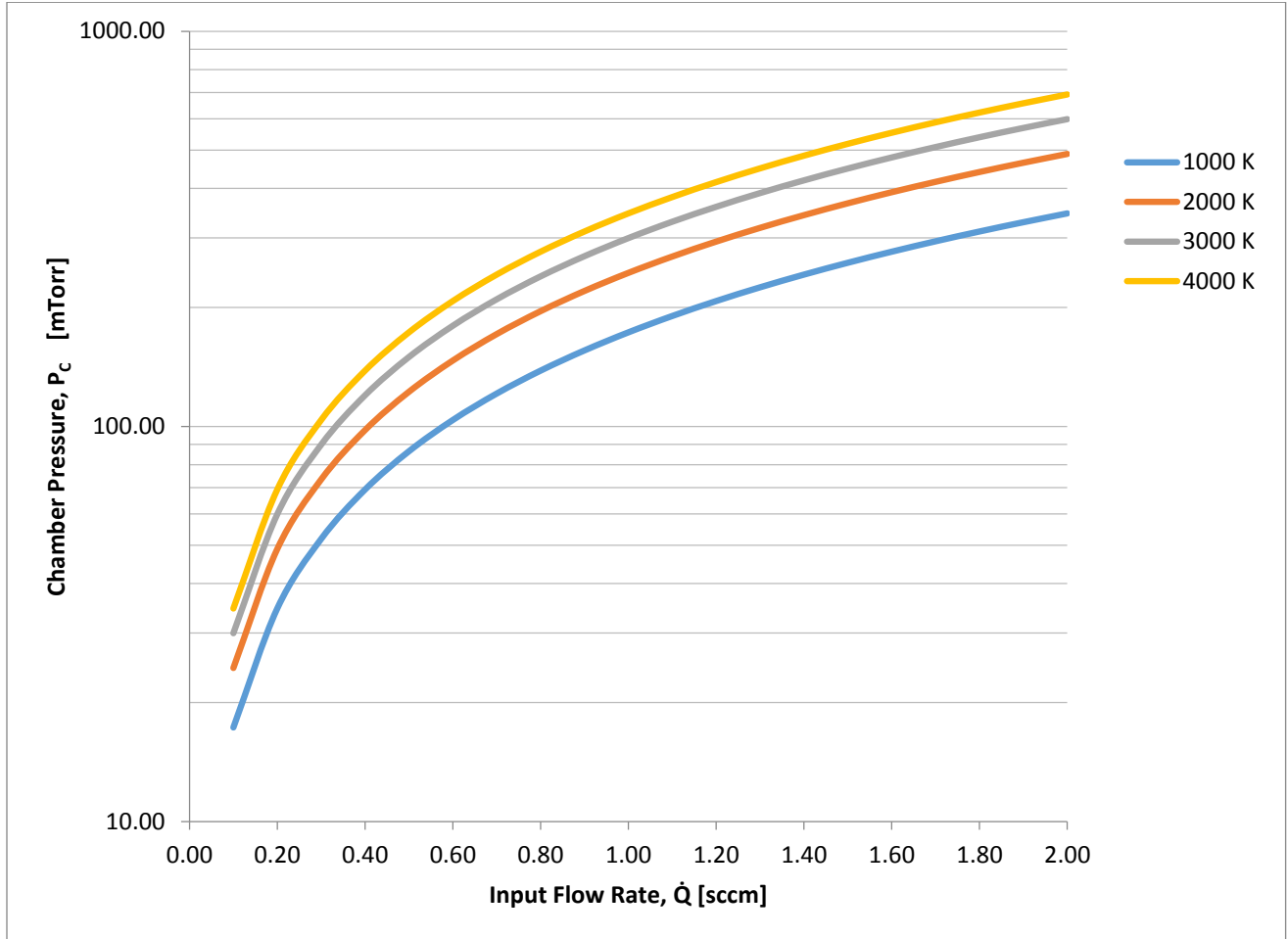
Figure 37. Discharge Chamber Pressure vs. Input Flow Rate at Various Discharge Chamber Temperatures.

A more comprehensive plotting operation was completed using a modified version of this Excel tool, resulting in a plot which included an expanded temperature range and a separate trend line for the pressure expected within the vacuum chamber (in contrast to the discharge chamber). The latter alteration was made by including the data retrieved from the chamber pressure versus flow rate test in the plot. Used throughout this project strictly for reference purposes, this plot is included in this report as Appendix E.

3.6 System Integration

Before working on an overall plan for system integration, the measurements were taken to determine relevant dimensions of the matching network enclosure, thruster, and T4 chamber. T-slotted framing was purchased to be used for fabrication of the RFET stand. Throughout the process of part selection, CAD renditions of each object were created and updated in SolidWorks to help finalize decisions on what parts to order while planning for fabrication and assembly.

3.6.1 Mechanical Integration

The T4 chamber and matching network enclosure were measured to make a CAD model of each object, allowing for an early idea of how the RFET stand and matching network enclosure could be positioned in the chamber. This initial layout, using the stand and RFET model provided by the 2015 RFET team [1], can be seen in Figure 38.
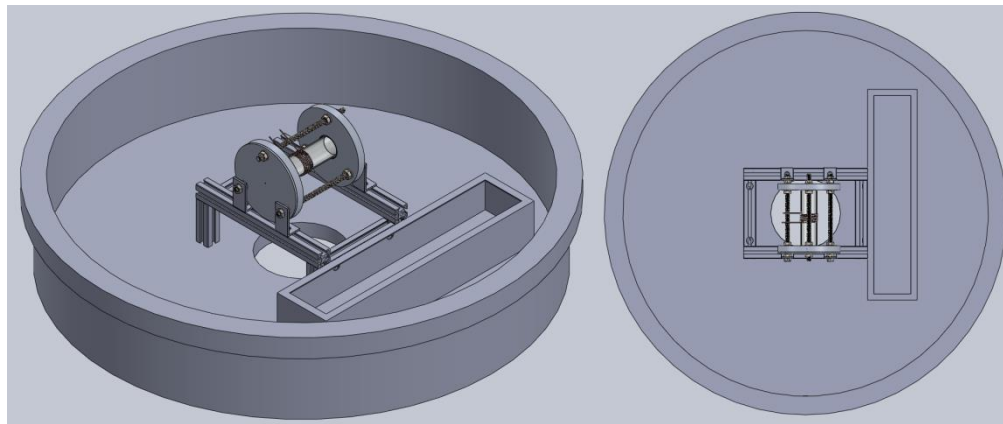
Figure 38. Isometric and Top View of Stand and Matching Network Inside Chamber.

The design of the stand was altered so that there was an equal distance of 6 inches between each of the stand legs. This decision was made so that, when attaching the matching network to the stand, the orientation of the thruster and the position of the matching network would be independent of each other. Additionally, by using corner-brackets to attach the matching network enclosure to the RFET stand, the installation and removal of the stand would be more convenient. The models were updated accordingly. With this change, the internal

components of the matching network would not need to be disturbed if the enclosure had to be moved.

Once the models were updated, holes were drilled in the matching network box for the corner-brackets, and t-slotted framing was ordered from McMaster-Carr for use in the assembly of the RFET stand. The thruster stand CAD models were updated to include models of the t-slotted framing that was purchased [24]. The fully updated assembly can be seen in Figure 39.
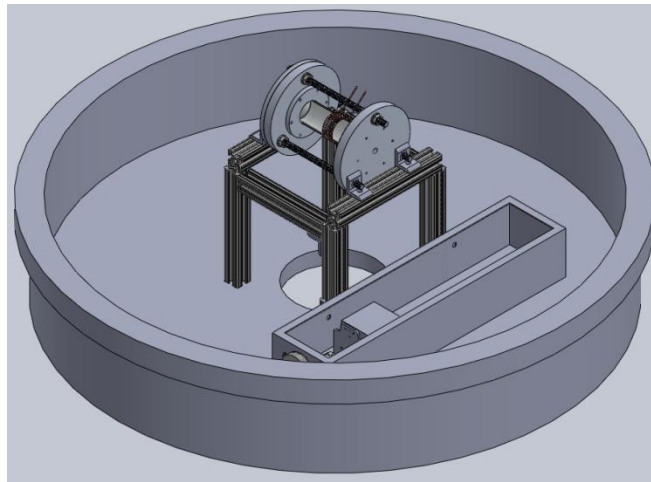
Figure 39. Stand and Matching Network CAD Assembly.

Before cutting the t-slotted framing, the required stand height for the thruster to be visible through the vacuum chamber window was determined. To accomplish this, the chamber was closed and a laser pointer was supported such that the laser was directed through the center of the viewing window. Once that was done, the chamber was opened and the distance from the bottom of the chamber to the laser was measured. Through this method, it was determined that the center of the chamber would need to sit at a height of 9.5 inches, requiring the legs of the stand to be 7.81 inches tall. The SolidWorks model was adjusted appropriately. With all the planning completed, the t-slotted framing was cut and milled in one of WPI's machine shops, and the stand was assembled, shown in Figure 40.

Figure 40. Assembled Stand Attached to Matching Network Enclosure

3.6.2 Electrical Integration

Electrical integration for the system required determining a method of controlling capacitance from outside of the vacuum chamber. With the ultimate intent of using a motor to turn the variable capacitor, the external geometry of the capacitor, which would be placed inside the matching network enclosure, was measured and reproduced in SolidWorks. The CAD model was used in order to have an estimate of how the capacitor could be integrated into the matching network. While measuring the dimensions of the variable capacitor, the torque necessary to turn the capacitor was also found by connecting a moment arm to the capacitor's shaft and adding mass until the shaft rotated.

An electrical switch was purchased from Jameco to control the motor, and hence the capacitance, within the matching network. A double-pole, double-throw switch which was momentary on-off-on was found. These switch attributes would allow the motor to only operate when the switch was moved from the neutral position, and rotate in opposite directions for each of the two non-neutral positions [23]. The switch was mounted on the control panel near the T4 chamber, due to the close proximity to the power source and chamber. To mount the switch to the control panel, a 0.0625 in thick sheet of aluminum was used to serve as the switch mount. The holes on the control panel that would be used to connect the switch mount were measured, and then the aluminum sheet was sheared and drilled. The switch is shown attached to control panel in Figure 41.

Figure 41. Switch mounted to Control Panel.

Once the motor arrived, a caliper was used to measure its various dimensions in order to create an accurate model in SolidWorks. Instead of using a bracket or mount of some kind, it was determined that it would be simpler, cheaper, faster, and just as effective to mount the motor directly to the side of the matching network enclosure, and updated the matching network CAD model to include holes for accommodating the motor. Before holes could be drilled, Teflon was used to isolate the capacitor, as discussed previously. As a result, the matching network chassis holes for the motor were repositioned in SolidWorks and then drilled. The motor was then mounted to the matching network enclosure as shown in Figure 42.
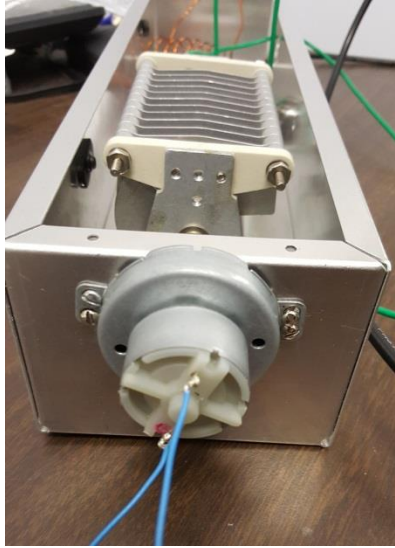
Figure 42. Motor Attached to Matching Network Enclosure.

For the wire connection between the switch and power supply, banana plugs were used to connect to the power supply and quick connects were used on the other end for connecting to the switch. For the wire connection between the switch and vacuum chamber, BNC connections were used to connect to the vacuum chamber feedthrough, and quick connects were used to connect to the switch. Inside the chamber, a pair of wires was already soldered to the electrical feedthrough posts. Quick connects were attached to the end of these wires which could then be connected to the matching quick connectors attached to wires soldered directly to the motor. Since connections between the switch and vacuum chamber feedthrough were being made with BNC connectors, RG-58 coaxial cables were used in the fabrication of the wires. The completed wires and cables with their connectors are shown in Figure 43.

Figure 43. Completed Wires.

The completed final assembly for the electrical integration (with the matching network outside of the vacuum chamber) is shown in Figure 44.
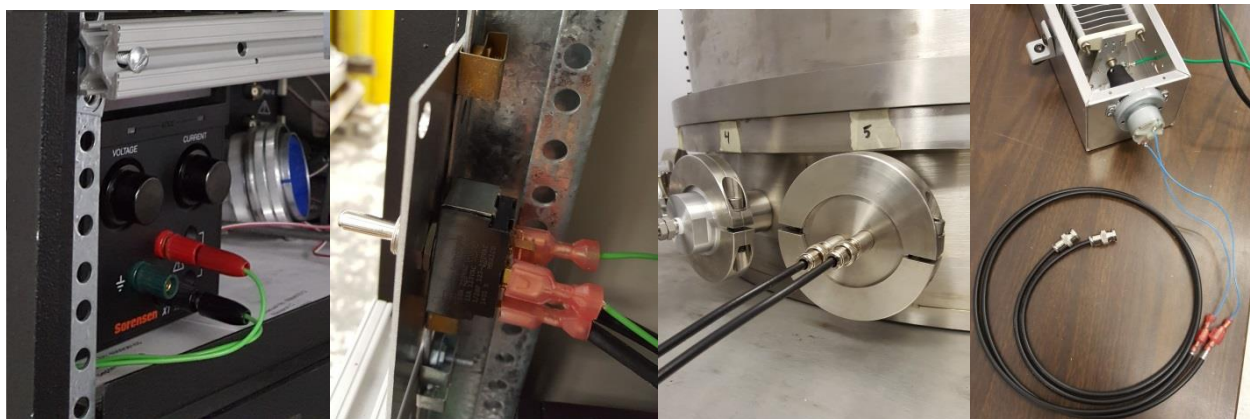
Figure 44. Leftmost: Connection to Power Supply; Middle Left: Switch Connections; Middle Right: Connection to Vacuum Chamber Feedthrough; Rightmost: Motor Connections.

After configuring the wires, the connection was tested with an ohmmeter and continuity was verified. Once the wires were fully connected to the matching network and motor, the switch, cables, and motor were tested to verify that they all operated as expected once connected to a power supply. With the power supply set to 5.7 volts, the motor turned the capacitor; flipping the switch resulted in the motor rotating in the opposite direction, as expected. With this test, the wires, switch, and motor were all determined to be successfully operating.

3.7 Final Thruster Testing

The thruster, with the gas discharge chamber tube secured within its mechanical structure, was mounted on the stand such that it was visible through the vacuum chamber observation window. Argon gas flowed through the discharge chamber, and the antenna, connected to the matching network, was coiled around the chamber tube. The matching network chassis was mounted on the thruster stand as well. The main purpose of the final test was twofold: 1) collect experimental data on the matching network and optimize its performance and 2) generate plasma that results in discharge of the propellant gas through the throat drilled in the nozzle plate.

The possible capacitor and inductor combinations for the matching network consisted of nine cases selected to cover a range of operating conditions (see Table 2). The fixed inductors can be configured in a variety of ways to nearly meet the required inductance for each case. For example, Case A requires a total of approximately 3.53 µH. Therefore, five 3.0 µH inductors can be used to achieve a value of 3.5 µH (see Figure 45). For Case B, the value of 3.2µH can be nearly achieved using seven 3.0 µH inductors in a different configuration (see Figure 46). Eqs. 16 and 17 were used to find equivalent inductances for components combined in series and parallel, respectively, where L_n is the inductance value of each component [21].

$$L_{Total} = L_1 + L_2 + \cdots L_n \tag{16}$$

$$L_{Total} = \left(\frac{1}{L_1} + \frac{1}{L_2} + \cdots \frac{1}{L_n} \right)^{-1} \tag{17}$$
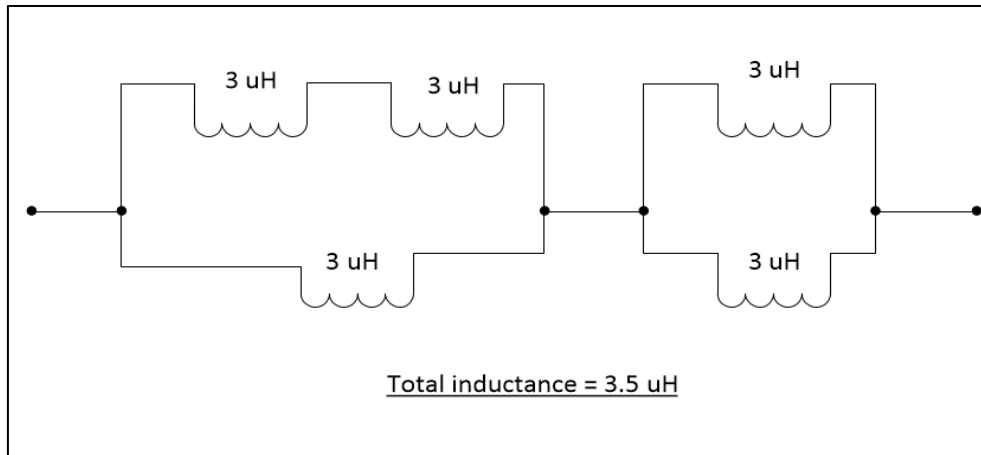
Figure 45. Inductor Configuration for Case A.
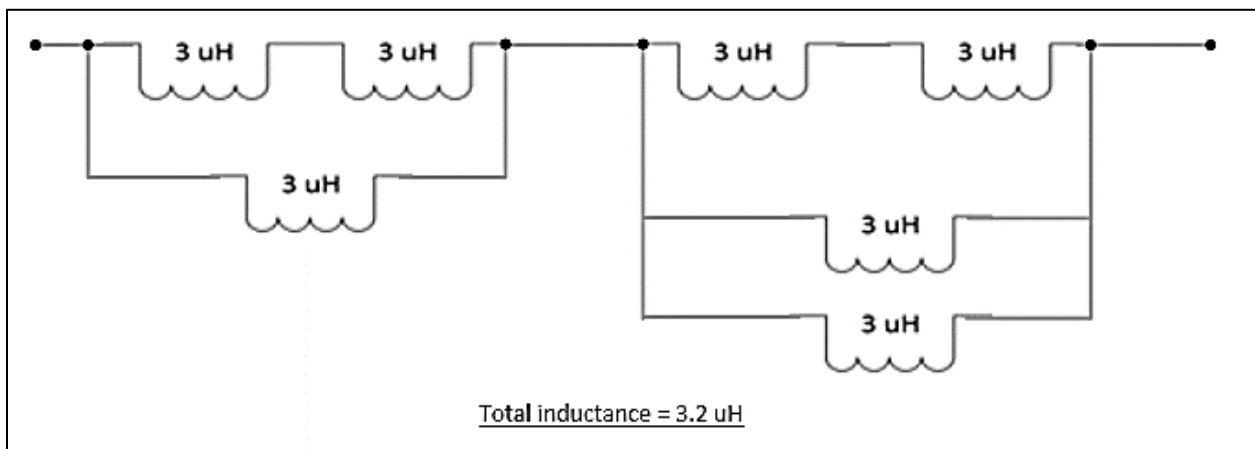
Figure 46. Inductor Configuration for Case B.

Due to time constraints, only initial testing to assess functionality of the fully integrated thruster was completed. For the preliminary test only, the "Maximum Power Allowed"[2] was 250 W, the gas flow rate was 0.5 sccm, and the inductor arrangement for Case B was installed in the matching network with the variable capacitor used for tuning. The capacitor was connected in series with the power source and the arrangement of inductors was connected in parallel with the

---

[2] The Maximum Power Allowed (MPA) is an agreed upon maximum (forward) power value to be attempted in a given test. For the initial test, it was assumed that if no discharge occurred with a power of 250 W, then there must be some problem needing further investigation.

load (i.e. antenna coil). The other end of the antenna coil returned to the power source via the outer shield conductor of the coaxial cable connected to a type-N port located at the rear of the transmitter. With the impedance matching network integrated, the RFET electrical circuit was then complete.

After ensuring all electrical safety precautions were in place (i.e. proper grounding of the RFET stand, matching network enclosure, and the chamber as a whole), the power supply was connected and turned on. Throughout testing, the variable capacitor was able to be slowly adjusted by operating the motor and allowing the impedance to settle after each adjustment. The RF power source has an analog dial on the front panel which indicates forward or reflected power. The reflected power was monitored while adjusting the capacitance. Additionally, the thruster was observed through the vacuum chamber window to monitor plasma generation. After recording sufficient data, the test procedure could then be repeated for the next test case. Due to time constraints, further testing was not conducted. Using this report for instruction, fabrication and testing of cases beyond this preliminary experiment can be completed.

4. RESULTS & DISCUSSION

The thruster assembly constructed by the 2015 RFET team [1] was found to have a sealing flaw that needed to be corrected. Therefore, immediate emphasis was placed on design and fabrication of an alternative mechanical thruster assembly, including a means by which to integrate the assembly into the T4 vacuum chamber. A new thruster, featuring a practical O-ring retainer system for proper sealing of the discharge chamber tube, was successfully designed and constructed. An interchangeable nozzle plate was also successfully incorporated into this redesign, better enabling future research regarding RFET thrust and exhaust plume analysis.

Additionally, a custom thruster stand was designed and constructed to integrate the thruster into the test chamber, and to make it viewable through the chamber's observation window. Furthermore, a complete impedance matching network was designed and assembled to couple the RF power provided to the load. The matching network is tunable via a remote control, DC motor, despite the entire network assembly being confined within the depressurized vacuum chamber.

Particular attention was devoted to ensuring that the thruster, matching network, and stand subassemblies remained compatible with one another throughout each step of design and construction. This attention to detail resulted in successful integration of the complete assembly (thruster, matching network, and stand) into the vacuum chamber and, ultimately, successful testing of the RFET.

While testing of the thruster was limited by time constraints, initial tests resulted in successful generation of plasma within the discharge chamber tube. The conditions at which this initial test was executed included an injected argon flow rate of 0.5 sccm and a pre-set maximum power of 250 W. The discharge became visible as soon as the RF generator was enabled, even with the power set point knob at its lowest value (i.e. zero). This suggests that the panel meter is either too coarse an indicator for low power levels or there was some other interaction occurring which affected the displayed value. Throughout this test, results were recorded using the value dialed in on the power set point control knob. It is estimated that the applied power level (i.e. forward power from the RF source) ranged between 50 and 85 W although there is no way to

confirm this without a dedicated power meter[3]. Although these results were primarily qualitative, the physical appearance of the plasma alone provided adequate results for preliminary analysis and discussion.

At lower power levels, characteristics of capacitive "E" mode discharge were observed. Mainly, the "hourglass" shape, with evident plasma concentration at either end of the chamber and narrowing at the center, as shown in Figure 47, indicated that the thruster was in E mode. Turning the capacitor by means of the motor, and thereby changing the capacitance of the matching network, caused the discharge to both dim out to extinction and re-ignite. This noticeable change served as evidence that the matching network was indeed altering the impedance and functioning as expected.
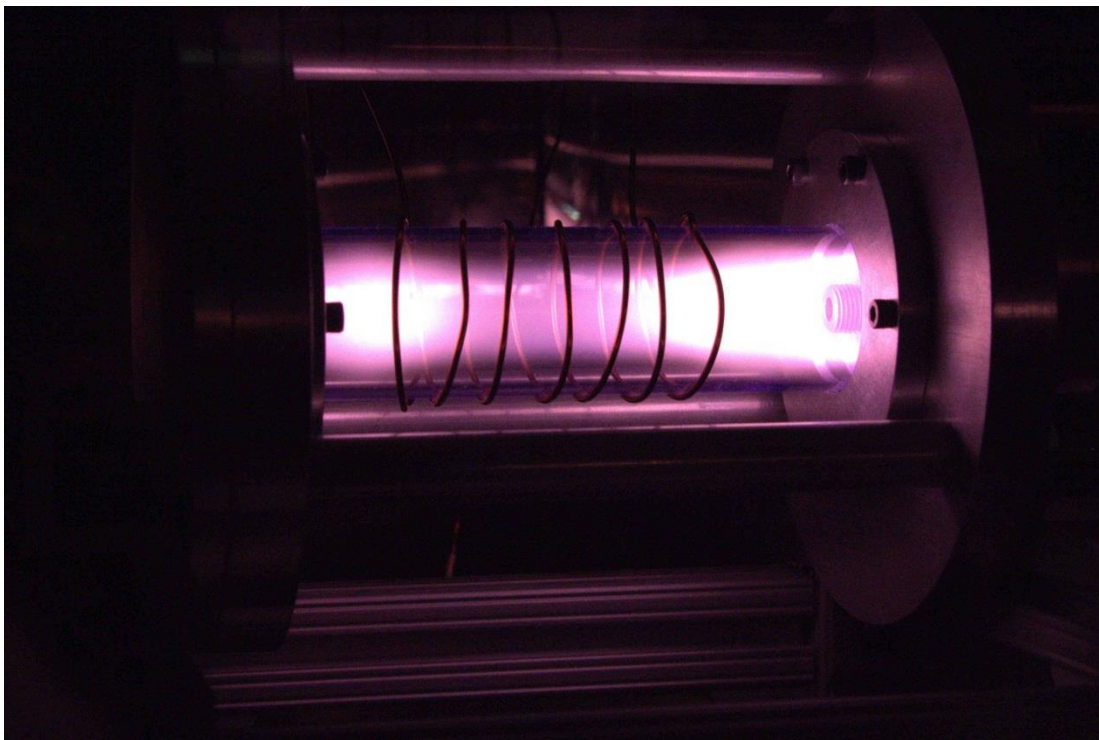
Figure 47. RFET Operating in E Mode.

As the power level was increased, characteristics of inductive "H" mode discharge were observed. The cylindrical shape, more uniform distribution throughout the chamber tube, and

---

[3] The estimate of 50 – 85 W was based on previous tests of the RF supply (without a plasma) in which the panel indicator moved noticeably when the set point knob was adjusted. This allowed a determination of forward power as a function of control set point.

greatly increased luminosity of the plasma, as shown in Figure 48, were indicative that the thruster was in H mode. Once H mode had been established, changing the capacitance of the matching network caused dimming and brightening of the discharge, much as it did for the case of the E mode discharge. At this high power case, however, changing the capacitance also resulted in transition between H and E modes. Additionally, by adjusting the capacitance while at the highest power setting, it was observed that the needle on the reflected power dial deflected noticeably. More specifically, the reflected power reading decreased at the moment the discharge transitioned from E to H mode.
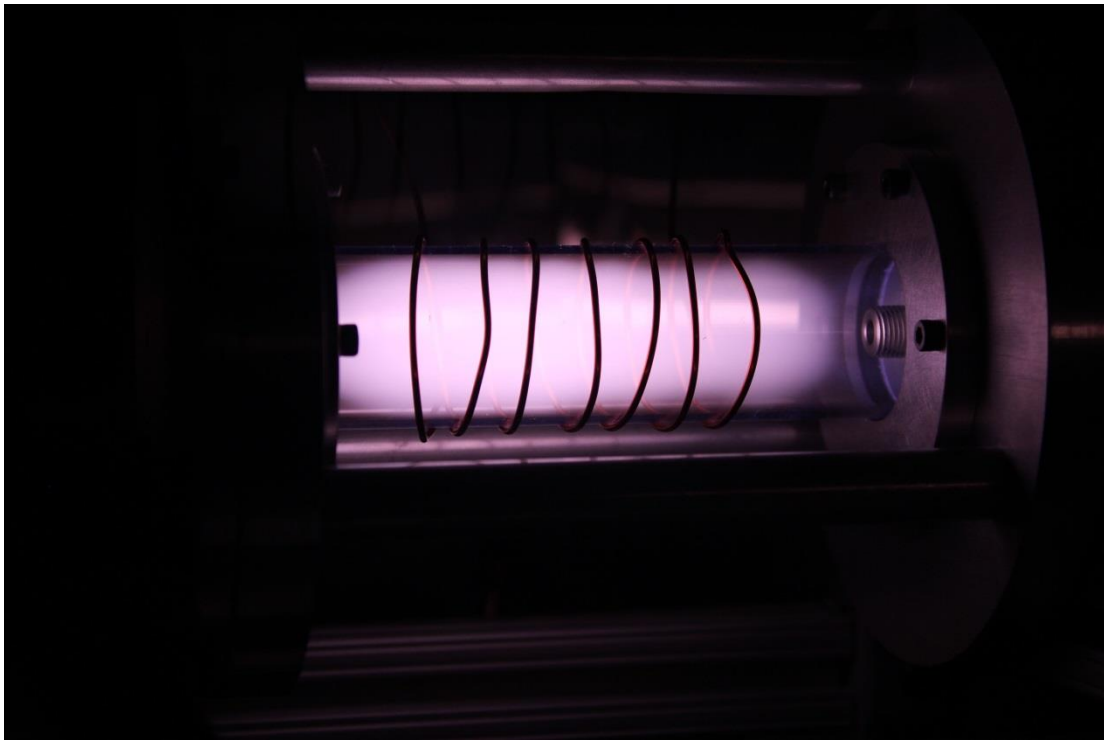
Figure 48. RFET Operating in H Mode.

To better test the E and H mode distinction, power was decreased after having established H mode discharge. It was found that the power could be decreased far below the level required to cause the E to H mode transition before the transition from H to E mode occurred. This observation served as further evidence that both E and H modes had been successfully initiated, since this behavior exhibited the anticipated hysteresis phenomenon. Verification of this phenomenon concluded our initial test for functionality of the RFET.

5. CONCLUSION & RECOMMENDATIONS FOR FUTURE WORK

The Design and Test of a Radio-Frequency Electrothermal Thruster MQP was initiated to complete the fabrication and testing of an RFET system. Picking up where the 2015 RFET team [1] had left off, five goals were established to define the course of action for completion of the project:

1. Update the RFET design to improve the discharge chamber sealing system;
2. Fabricate an RF antenna;
3. Design and construct an impedance matching network ;
4. Integrate the RFET assembly systems for testing; and
5. Test the fully integrated RFET assembly.

Initially, it was planned that minimal changes to the thruster would be made for improvement of the discharge chamber tube seal. However, the best way to improve the thruster design of the 2015 MQP required unavailable tools. Therefore, the thruster was completely redesigned and fabricated it according to this new design. By redesigning the thruster, goal of improving the seal was completed.

For the RF antenna, difficulties were encountered in designing an antenna coil without knowing the impedance of the plasma load. Using the concept of equivalent circuits, and referring to previous suggestions from outside sources, the number of turns to use for the coil was estimated. Therefore, the goal of creating an RF antenna appropriate for the expected operating conditions of our RFET was completed.

The matching network proved to be the most difficult of the four goals. The process of completing the matching network was slowed by receiving conflicting information from various sources, as well as a lack of documentation for matching network designs under similar circumstances. After completing many iterative design processes, a solution for this particular project was found. Once the design was solidified, the matching network was successfully constructed.

Assembly integration was a very broad goal, but had specific focus on a few select requirements. One requirement was that the RFET had to be visible through the vacuum

chamber's viewing window. Also, the matching network chassis needed to be placed within the vacuum chamber in such a way as to permit connection to the antenna. Since the matching network implemented a variable capacitor, a method was devised for controlling a motor to change the capacitance from outside of the chamber. To meet these requirements, a stand was designed and fabricated such that it would hold the RFET at the desired height and provide a mounting space for the matching network. A motor and switch were purchased and integrated to address the variable capacitance needs. By the conclusion of this project, the thruster mechanical assembly, matching network, and thruster stand had all been successfully integrated into the vacuum chamber, and all assemblies were prepared and readied for commencement of testing procedures. Finally, the fully-constructed RFET was successfully tested with positive results. As a result, the goals of system integration and testing, and thereby the overall goal for the project, was successfully completed.

While electric propulsion is an attractive technology option for space exploration, this particular RFET will provide future opportunities for research at WPI. The next step for this RFET is to complete further testing over a wider range of power and flow rate. Due to time constraints, the team was prevented from completing the additional test cases, but further testing can be easily conducted by future teams. If this project is to be continued beyond the final test as another WPI MQP, it is recommended that electrical engineering students optimize the matching network. If this is not practical, another option is to use a commercially available, automatic matching network. Since the power level is relatively low, these are widely available, marketed as automatic "antenna tuners" used by ham radio enthusiasts. The matching network was, by far, the most challenging component of this project because it presented subject matter that is not included in the general aerospace course load. Therefore, future students could build off of this thruster and determine the most efficient and accurate way to match the impedance of argon plasma generated by an RF antenna. Additionally, even though integrating a diverging nozzle was outside the scope of this major qualifying project, implementation was still considered. However, due to time and manufacturing constraints, the design and fabrication of an optimized nozzle was not explored in significant detail. While a constant diameter throat was sufficient for the proof of concept demonstrated in this project, a converging-diverging nozzle would allow for more representative thrust generation and specific impulse to be realized in future tests. Therefore, it is recommended that future efforts investigate the design and implementation of a

nozzle, either as an addition to or in place of the current throat. Beyond growth opportunities for the electrical and mechanical aspect, this thruster can be used for future graduate research at WPI, specifically plume analysis and thrust measurement.

REFERENCES

1. Byrne, R., S. Osborn, Z. Tripp, Design and Fabrication of a Radio-Frequency Electrothermal Thruster, WPI, JB3-1502, (2015).

2. Callen, J.D. Fundamentals of Plasma Physics [online] 2003. Available from http://physics.bgu.ac.il/~gedalin/Teaching/Mater/plasma3.pdf. Accessed 11/12/2015.

3. Ehlers, E.G. Phase: State of matter [online] 2011. Available from: http://www.britannica.com/science/phase-state-of-matter. Accessed 12/07/2015.

4. SSE. Arcjets [online] 2015. Available from: http://www.lr.tudelft.nl/en/organisation/departments/space-engineering/space-systems-engineering/expertise-areas/space-propulsion/propulsion-options/thermal-rockets/arcjets/. Accessed 10/02/2015.

5. B.T.C. Zandbergen. Resistojets [online] 2015. Available from: http://www.lr.tudelft.nl/en/organisation/departments/space-engineering/space-systems-engineering/expertise-areas/space-propulsion/propulsion-options/thermal-rockets/resistojets/. Accessed 10/02/2015.

6. Wallner, L.E., J. Czika. Arc-Jet Thrustor for Space Propulsion [online] 1965. Available from: http://ntrs.nasa.gov/archive/nasa/casi.ntrs.nasa.gov/19650017046.pdf. Accessed 12/15/2015.

7. Tacina, R. Conceptual Design and Integration of a Space Station Resistojet Propulsion Assembly [online] 1987. Available from: http://ntrs.nasa.gov/archive/nasa/casi.ntrs.nasa.gov/19870010945.pdf. Accessed 12/15/2015.

8. Chabert, P., Braithwaite, N. Physics of Radio-Frequency Plasmas [online] 2011. Available from: https://books.google.com/books?id=oB03j-bbNXcC&lpg=PA10&ots=g3ItlEaBgF&dq=radio%20frequency%20electrothermal%20thruster&pg=PP1#v=onepage&q&f=true. Accessed 10/20/2015.

9. [Anonymous]. Plasma Processing [online] 1993. Available from: http://www.plasma.impe.br/LAP_portal/LAP_Site/Text/Plasma_Processing.htm. Accessed 09/15/2015.

10. Zaplotnik, R., A. Vesel, M. Mozetic, Transition from E to H mode in inductively coupled oxygen plasma: Hysteresis and the behaviour of oxygen atom density, EPL Journal, 95, (2011).

11. Hopkins, J.R., M.M. Micci, S.G. Bilen. Design and Testing of a Low Power Radio-Frequency Electrothermal Thruster [online] 2009. Available from:

http://erps.spacegrant.org/uploads/images/images/iepc_articledownload_1988-2007/2009index/IEPC-2009-168.pdf. Accessed 10/20/2015.

12. Ahedo, E. Plasma dynamics in a helicon thruster [online] 2011. Available from: http://aero.uc3m.es/ep2/docs/publicaciones/ahed11e.pdf. Accessed 10/20/2015.

13. Charles, C., et al., Nanosecond Optical Imaging Spectroscopy of an Electrothermal Radiofrequency Plasma Thruster Plume, Applied Physics Letters, Vol. 103, (2013).

14. Lafleur, T, et al., Direct thrust measurements and modelling of a radio-frequency expanding plasma, AIP Publishing, Physics of Plasmas, Vol. 18, (2011).

15. Bezooijen et al., 'IEEE Transactions on Circuits and Systems', 0256698, 2012.

16. Wiliams et al., 'Method of an apparatus for independently controlling electric parameters of an impedance matching network', 5889252, 2015.

17. Armstrong Metalcrafts. AWG Copper Wire Properties [Data File]. Retrieved from: http://www.armstrongmetalcrafts.com/Reference/AWGCopperWireProperties.aspx

18. Colpo, P., Roland, E., and Rossi, F. "Determination of the equivalent circuit of inductively coupled plasma sources," Journal of Applied Physics, Vol. 85, No. 3, 1999.

19. Blattenberger, K. (n.d.). Dielectric Constant, Strength, & Loss Tangent. Retrieved March 04. 2016, from http://www.rfcafe.com/references/electrical/dielectric-constants-strengths.htm

20. Parker Hannifin Corporation. Parker O-Ring Handbook [online] 2007. Available from: https://www.parker.com/literature/ORD%205700%20Parker_O-Ring_Handbook.pdf. Accessed 10/02/2015.

21. [Anonymous]. "The ARRL Handbook", *The 88th Edition for Radio Communications,* CT, 2011

22. Todorow, V., "Impedance Matching and Matching Networks", *Etch Products Business Group, Applied Materials*, 2009, from: http://www.engr.sjsu.edu/rkwok/Engr297/Val_Impedance%20Matching%20and%20Matching%20Networks.pdf

23. [Anonymous]. Jameco. Product Listing [Online] 2015. Available from: www.jameco.com

24. [Anonymous].McMaster Carr. Product Listing [Online] 2015. Available from: http://www.mcmaster.com

25. Kuphaldt, T. (n.d.) Lessons in Electronic Circuits [online] 2006. Available from: http://www.allaboutcircuits.com/assets/pdf/direct-current.pdf

26. Moore, J. Davis, C. Coplan, M. Building Scientific Apparatus (2nd Ed.). (1989).

27. Gonzalez, L. Khaled, N. Theriot, P. White, J. Optical Emission Study of a Pulsed Plasma Thruster (2014).

28. [Anonymous]. "Rocket Engine Plume Analysis". *Sierra Engineering.* 2012, from: http://www.sierraengineering.com/Plume/plume.htm

29. [Anonymous], "OEM-6 RF Plasma Generator," *ENI Service Manual*, USA, 1996

30. Long, S., "ECE145A/ECE 218A Notes Set #5", *ECE Department, University of California Santa Barbara*, 2007, Available from: http://www.ece.ucsb.edu/~long/ece145a/Notes5_Matching_networks.pdf

31. Envirotech Instruments Pvt. Lmd. Bubble-o-Meter™: Operation Instruction of Soap Bubble Meter.

32. Bubble-O-Meter (n.d.) [online] 2016. Available from: http://www.bubble-o-meter.com. Accessed 03/15/2016.

33. Pote, A. Space Grant Summary 2008, Summary Abstract and Statement, 2008.

34. Hall, N. Mass Flow Choking [online] 2015. Available from: https://www.grc.nasa.gov/www/k-12/airplane/mflchk.html. Accessed 02/01/2016.

APPENDICES

Appendix A

%%Prepared by J. Blandino

% Matching Network Calculation

%define the equations using a .m function

%% Setup

clear all; clc;

global XL RL Rg

%% Solve the equations:

% initial guess

aguess=100; bguess=100;

%

freq=13.56e6;   % source frequency [Hz]

% write initial guess in a vector form

xguess=[aguess, bguess];

% Solve the equations, calling the function 'funmaths'

%with the 2 equations to be solved

x=fsolve('funmaths', xguess);

%

%Displays the results for Xs, Xp and other intermediate variables used in the solution

Xs=x(1)

Xp=x(2)

%

a=-Xp*XL;

b=Xp*RL;

c=RL;

d=Xp+XL;

e=(a*c+b*d)/(c^2+d^2);

```
f=(b*c-a*d)/(c^2+d^2);
%
Re_ZT=e
Im_ZT=f+Xs
%
 if Xs > 0
     L=Xs/(2*pi()*freq)
    else
     C=(-1.0)/(2*pi()*freq*Xs)
 end
%
 if Xp > 0
     L=Xp/(2*pi()*freq)
    else
     C=(-1.0)*1/(2*pi()*freq*Xp)
 end
```

Appendix B

```
function y=funmaths(x)
% Matching Network Calculation
%J. Blandino
%This is a function file that must be placed
%in the same folder as "maths.m"
global XL RL Rg
%
Xs=x(1);
Xp=x(2);
XL= 450;
RL= 400;
Rg= 50;
%


a = @(Xs,Xp)  -Xp*XL;
b = @(Xs,Xp)  Xp*RL;
c = RL;
d = @(Xs,Xp)  Xp+XL;
e=  @(Xs,Xp)  (a(Xs,Xp)*c+b(Xs,Xp)*d(Xs,Xp))/(c^2+d(Xs,Xp)^2);
f=  @(Xs,Xp)  (b(Xs,Xp)*c-a(Xs,Xp)*d(Xs,Xp))/(c^2+d(Xs,Xp)^2);


% System of 2 equations to be solved simultaneously.
y(1,1) = e(Xs,Xp)-Rg ;
y(2,1) = f(Xs,Xp)+Xs ;
%
```

Appendix C

```
%%Prepared by J. Blandino
% Matching Network Calculation
%define the equations using a .m function


%% Setup
clear all; clc;
global XL RL Rg
%% Solve the equations:


% initial guess
aguess=150; bguess=300;
%
freq=13.56e6;    % source frequency [Hz]
% write initial guess in a vector form
xguess=[aguess, bguess];


% Solve the equations, calling the function 'funmaths'
%with the 2 equations to be solved
options = optimset('MaxFunEvals',500);
x=fsolve('funmaths2', xguess,options);
%
%Displays the results for Xs, Xp and other intermediate variables used in
%the solution
%
%
Xs=x(1)
Xp=x(2)
%
a=-Xp*Xs
b=Xp*Rg
c=Rg
```

```
d=Xp+Xs
e=(a*c+b*d)/(c^2+d^2)
f=(b*c-a*d)/(c^2+d^2)
%
Re_ZT=e
Im_ZT=-f
%
 if Xs > 0
     L=Xs/(2*pi()*freq)
    else
     C=(-1.0)/(2*pi()*freq*Xs)
 end
%
 if Xp > 0
     L=Xp/(2*pi()*freq)
    else
     C=(-1.0)*1/(2*pi()*freq*Xp)
 End
```

Appendix D

```
function y=funmaths2(x)
% Matching Network Calculation
%J. Blandino
%This is a function file that must be placed
%in the same folder as "maths.m"
global XL RL Rg
%
Xs=x(1);
Xp=x(2);
XL= 215;
RL= 145;
Rg= 50;
%


a = @(Xs,Xp)  -Xp*Xs;
b = @(Xs,Xp)  Xp*Rg;
c = Rg;
d = @(Xs,Xp)  Xp+Xs;
e=  @(Xs,Xp)  (a(Xs,Xp)*c+b(Xs,Xp)*d(Xs,Xp))/(c^2+d(Xs,Xp)^2);
f=  @(Xs,Xp)  (b(Xs,Xp)*c-a(Xs,Xp)*d(Xs,Xp))/(c^2+d(Xs,Xp)^2);


% System of 2 equations to be solved simultaneously.
y(1,1) = e(Xs,Xp)-RL ;
y(2,1) = f(Xs,Xp)+XL ;
%
```

Appendix E

Discharge Chamber Pressure and Vacuum Pressure vs. Input Flow Rate at Various Discharge Chamber Temperatures
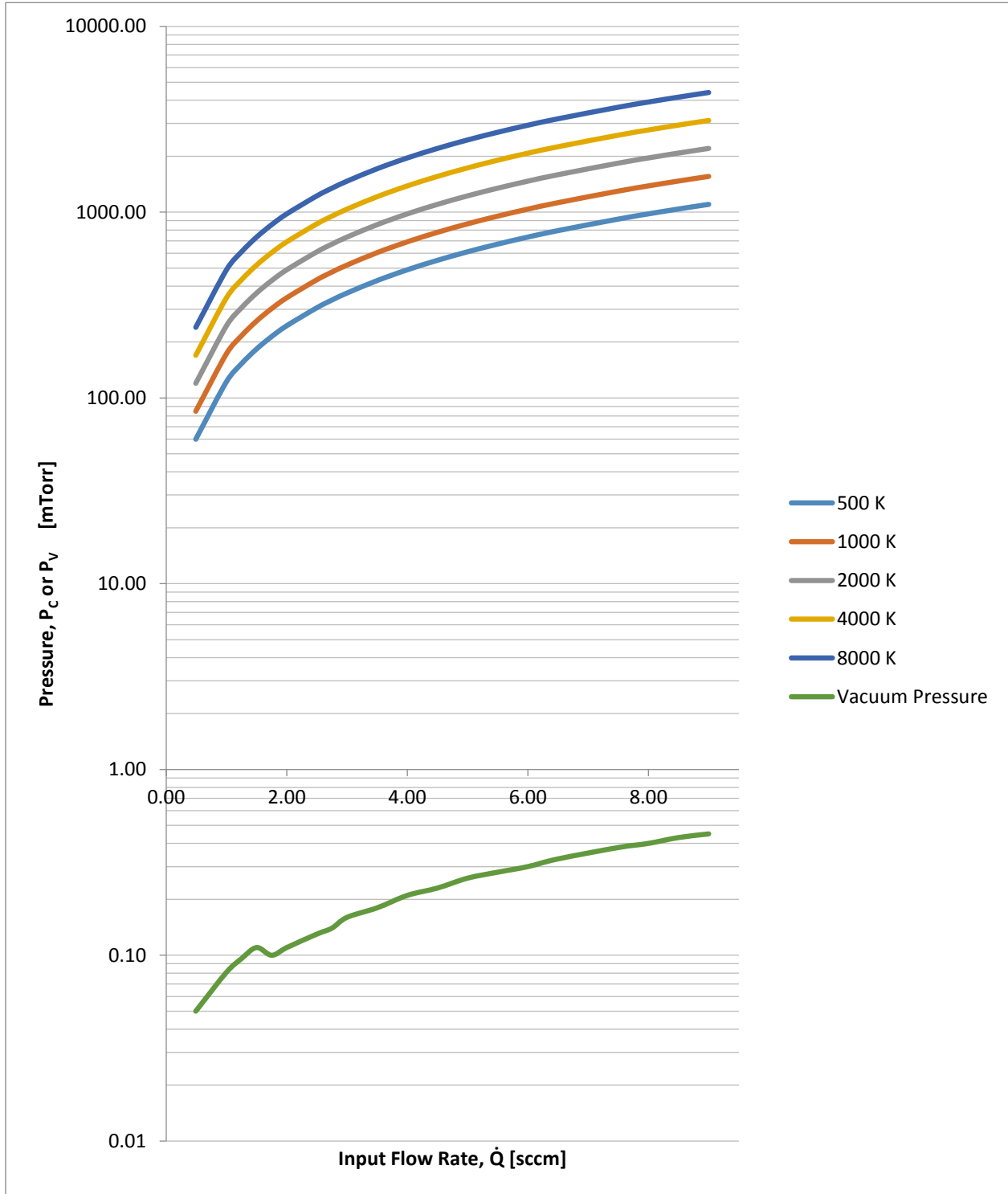
Appendix F

Key Component Breakdown

Vendor	Model/Part Number	Item Description	Qty.	Unit Price	Total Price
MCS	02255743	Aluminum Plates | Material: Aluminum | Thickness (Inch): 1/2 | Width (Inch): 12 | Length (Inch): 12 | Alloy Type: 6061	1	$71.95	$71.95
MCS	02255669	Aluminum Plates | Material: Aluminum | Thickness (Inch): 1/4 | Width (Inch): 12 | Length (Inch): 12 | Alloy Type: 6061	1	$41.48	$41.48
Jameco	2182004	Switch Rocker DPDThrow Mom-Off-Mom .4@20	1	$0.69	$0.69
Jameco	18922	Case ABS Speedy 3.125x2x.875	1	$3.49	$3.49
Jameco	621683	Toggle Switch (On)-Off-(On) DPDT Bat Lever Quick Connect 15A 250VAC Panel Mount	1	$18.95	$18.95
McMaster-Carr	6410K53	Over-Torque-Prevention Vibration-Damping Coupling, 1/4" x 5/16" Diameter Shaft, 1" OD	1	$24.10	$24.10
McMaster-Carr	94701A239	PTFE Machine Screw Pan Head Slotted, 6-32 Thread, 3/4" Length	2	$4.46	$8.92
McMaster-Carr	9711K11	Extreme-Temperature Slippery PTFE Sheet Tight-Tolerance 1/4" Thick, 2" x 12"	1	$38.03	$38.03
McMaster-Carr	95630A236	PTFE Flat Washer Number 5 Screw Size, 0.145" ID, 0.500" OD	1	$4.03	$4.03
Newark	Newark Part # 53W3028 / Mfg Part # M22759/11-12-9	Wire, Hook Up, Mil M22759, Per Ft, 12 AWG, 600 V, White	5	Free Sample	$0.00
Coilcraft	Coilcraft Part # XAL1350-302_E_	3.0 uH XAL1350 Series Shielded Power Inductors, 74 A, 1.50 mOhms DCR, tin/silver core	8	$5.51	$44.08
RF Parts	RF Parts # 154-14-15	154-14-15 Air Variable Capacitor, 16-101 pf, 4.5 kV (explicitly high rated?)	1	$49.95	$49.95
Techni-Tool	319SO725 / Mfg Part # SMDSWLF .0312OZ	ChipQuik Wire Solder, 0.031" Dia., SACE305, 2 oz. Spool	1	$11.47	$11.47